Acta Astronautica 172 (2020) 16–32

Contents lists available at ScienceDirect

Acta Astronautica

journal homepage: www.elsevier.com/locate/actaastro

# Speckle noise attenuation in orbital laser vibrometer seismology

Samuel W. Courville*, Paul C. Sava

*Colorado School of Mines, Center for Wave Phenomena, 1500 Illinois St, Golden, CO, 80401, USA*

ARTICLE INFO

*Keywords:*
Asteroid interiors
Seismology
Laser vibrometry
Laser speckle

ABSTRACT

The interior structures of small planetary bodies such as asteroids and comets are an enigma. Determining the internal structure is important for understanding the formation and evolution of the solar system and also has implications for in-situ resource exploitation and planetary defense. Despite the immense value, no detailed investigation of the interior properties of an asteroid has yet been made. Although orbital radar and lander based seismological approaches have been proposed to make direct interior observations, it has not yet been demonstrated that radar could transmit through a rocky asteroid, nor that landing multiple seismometers is feasible or affordable. An elegant alternative to landed seismometers is orbital laser Doppler vibrometry, which could record seismic shaking of a small body without contact with the surface. Laser Doppler vibrometers (LDVs) are mature instruments for terrestrial applications and could be adapted for a space environment. However, when incident on a rough surface like an asteroid regolith, an LDV is subject to laser speckle noise which may be misinterpreted as seismic shaking. We address the challenge of making LDV measurements on naturally rough surfaces by quantifying the laser speckle noise that an orbital LDV would encounter during a hypothetical orbital measurement. Specifically, we simulate an LDV measurement of a seismic signal generated by an impact source on the asteroid 101955 Bennu. We demonstrate that speckle noise can be attenuated by combining multiple signals recorded by an orbital seismometer equipped with multiple LDV sensors. By mitigating laser speckle, we demonstrate that an orbital LDV can record seismic signals on a natural asteroid surface, which would enable an orbital seismometer to achieve the dense global coverage necessary for high resolution interior imaging.

## 1. Introduction

Small planetary bodies such as asteroids and comets are the building blocks of the solar system. Understanding how they form is key to understanding how the solar system formed and evolved [1,2]. Small planetary bodies are akin to laboratories where we can test hypotheses of planetary accretion, from the particle scale upward. Questions about the origin of small bodies and planetary accretion often come down to understanding their internal structure [1,2]. For example, there are several credible hypotheses for the interior structure of asteroids: rubble piles composed of gravitationally bounded impact shards, fractured monoliths that have remained largely intact despite impacts, or compactable fluffy regolith balls [1–3]. Likely, the answer differs by asteroid type, and implies differing early solar system formation environments. In addition to scientific pursuits, knowledge of asteroid interior properties could also be useful for in-situ resource utilization. Lastly, questions about the interior structure of asteroids are also important for planetary defense. Knowledge of their interior structure is required to deflect or disrupt asteroids on collision courses with Earth [4].

Our understanding of asteroid and comet interiors has significantly improved in recent years largely due to surface observations from recent missions [2]. Over two dozen asteroids and comets have been visited by spacecraft to date, and another dozen are expected to be visited by spacecraft in the next decade [5]. Among the recent missions, NASA's Origins, Spectral Interpretation, Resource Identification, Security, Regolith Explorer (OSIRIS-REx) is exploring asteroid 101955 Bennu, which is now interpreted as a rubble pile through topographic and image analysis [6]. Data from JAXA's Hayabusa2 spacecraft, including analysis from an impactor experiment that disrupted the near surface, suggests that asteroid 162173 Ryugu is also a rubble pile [7]. ESA's Rosetta mission to the comet 67P/ChuryumovGerasimenko revealed that the comet is likely a weakly layered agglomeration [8]. This interpretation is supported by bistatic radar data measurements, the only successful direct observations of a cometary interior to date [9]. Despite these impressive exploration advances, no detailed interior image of an asteroid's interior structure has been made [10,11]. Advances in numerical modeling allow for the development of internal structure hypotheses that can explain surface observations, but these hypotheses can not be tested without direct measurements. The interior

* Corresponding author.
*E-mail address:* swcourville@gmail.com (S.W. Courville).

https://doi.org/10.1016/j.actaastro.2020.03.016
Received 21 December 2019; Received in revised form 10 March 2020; Accepted 11 March 2020
Available online 19 March 2020
0094-5765/ © 2020 Published by Elsevier Ltd on behalf of IAA.

structure of small bodies remains terra incognita [1].

Recognizing the scientific value of making direct measurements of small body interior properties, various authors have proposed missions with sounding instruments to peer inside small bodies [2]. Building off of the bistatic radar experiments conducted by ESA's Rosetta mission, Asphaug et al. [12], Sava et al. [13], Sava and Asphaug [14], and Sava and Asphaug [15] have proposed radar imaging. Although radar waves can propagate several kilometers through icy material, they rapidly attenuate in solid rock [16]. This means that although radar may be a valid solution for imaging icy comets, it remains to be demonstrated that it is a viable option for imaging rocky asteroid interiors.

Seismology provides an attractive alternative to radar. Whereas radar is sensitive to electromagnetic properties, which may not be correlated to geologic structure, seismic waves are sensitive to properties such as density and compressibility, which are directly related to the interior structure and strength [11]. Richardson et al. [17] and Asphaug [18] have demonstrated that seismic waves propagating through asteroids, as generated by impacts, can cause global surface disruption. Using empirical and numerical models, the observed surface disruption can be related to the bulk interior properties [18]. However, this method is still an indirect interpretation of the interior. A more robust option is to directly observe seismic propagation through asteroids, for example using landed seismometers on an asteroid [19]. Landed seismometers could record seismic waves that have propagated through the center of an asteroid. However, this approach is technically challenging because multiple seismometers must land across the surface of the asteroid [19]. Additionally, it is unknown whether a seismometer resting on the surface of an asteroid would be coupled well enough to make useful seismic measurements [11].

Orbital seismology is a more elegant solution with significant advantages over lander based seismology. Instead of landing seismometers [11], propose to use laser Doppler vibrometers (LDVs) for non-contact remote sensing of seismic signals. By shining a laser on a vibrating object and recording the Doppler shift of the light that reflects back, an LDV can measure the velocity of the object. LDVs are well developed instruments that enjoy a wealth of applications on Earth such as structural health monitoring and manufacturing component testing [20–22]. Drbenstedt et al. [23] have provided experimental proof that an isolated and stationary LDV can record seismic signals. Further work by Halkon and Rothberg [24] suggests that a drone mounted LDV could collect vibration data remotely provided that the signal from the drone's motion can be removed. Correcting for motion as the drone actively holds itself in the air is the limiting factor for airborne seismic measurements [25]. However, a spacecraft would not be subject to such motion. We consider the possibility of recording seismic signals with an LDV mounted on a spacecraft. Equipped with an LDV, a spacecraft could achieve global seismological coverage of a small body without ever landing on the surface. Sava and Asphaug [11] show that LDV measurements of seismic signals at multiple locations over an asteroid's surface can make a 3D image of its interior properties.

Sava and Asphaug [11] propose that an orbital LDV could make non-contact seismic measurements of an asteroid, but do not address whether LDVs could function on natural asteroid surfaces, which is a key aspect of orbital seismology. Without the ability to operate on rough surfaces, LDVs could not achieve dense measurement coverage over a small body because coverage would be limited to wherever laser retroreflectors could be deployed across its surface. To reap the full benefits of an orbital seismometer, the instrument must be functional on natural surfaces. Whereas LDV's can achieve nm/s or better resolution in low noise settings, they are subject to so-called speckle noise when in motion relative to a rough target surface [26]. This noise is a result of constructive and destructive interference of light reflected by surfaces with roughness greater than the wavelength of the laser [27]. In this paper, we quantify laser speckle noise and design methods to separate it from seismic signals in order to bolster the orbital seismology concept proposed by Sava and Asphaug [11].

Through numerical simulations, we demonstrate that accurate seismic measurements in the presence of speckle noise are possible from an orbital LDV acting on natural asteroid surfaces. We first discuss the methodology needed to predict the speckle noise produced by orbital motion of an LDV over a rough natural surface. Next, we analyze characteristics of possible seismic signals that an LDV would need to record. There are several potential natural and artificial seismic sources to consider on a small body. Natural sources might include tidal forces inducing natural microseismic events, outgassing from a comet generating slight shaking, or the jolt from an impact [17,28]. The OSIRIS-REx mission has also observed particle ejection events at 101955 Bennu which could produce seismic sources [29]. Artificial sources could be based on chemical explosives as occasionally used in seismic exploration on Earth [30], or artificial impacts [31]. In our study, we focus on artificial sources given our greater ability to predict and control their location and magnitude. We specifically assume an impact source similar to the Small Carry-on Impactor (SCI) experiment on JAXA's Hayabusa2 mission, which demonstrated a plausible means to generate artificial seismic sources with a small spacecraft add-on [31]. Finally, using the signal and noise estimates, we show that speckle noise can be separated from the seismic signal through signal diversity combining. Thus, this paper is organized into three major sections addressing the questions:

1. What is the speckle noise inherent in an orbital measurement? (Section 2)
2. What is the seismic signal we expect to record from an impact source? (Section 3)
3. How do we separate the seismic signal from the speckle noise? (Section 4)

We demonstrate the separation of speckle noise from seismic signals, using a seismic data acquisition scenario over the asteroid 101955 Bennu (Fig. 1). We consider an LDV orbiting the asteroid at a distance of 2 km above the surface. Given the mass of 101955 Bennu, this yields an orbital velocity of approximately 5 cm/s, which is similar to the orbital velocity of OSIRIS-REx [32]. We assume that the laser spot point moves across the surface at the same speed as the spacecraft orbits. In reality, the spot might move slower or faster depending on the rotational velocity of the asteroid in relation to the chosen orbit. Lastly, we assume that a seismic impact source is located on the opposite side of the asteroid and is generated from an impactor similar to Hayabusa2's SCI.

## 2. LDV speckle noise simulation

### 2.1. LDV theory

In this section, we briefly review laser Doppler vibrometer (LDV) theory. An LDV measures the velocity of a target object by shining a laser on the object and recording the Doppler shift of the reflected laser light caused by the target's motion. LDVs are mature instruments, and a full description of how they function can be found in Donges and Noll [33]. An LDV uses a laser of known wavelength that is split into two beams. One beam remains in the LDV as a reference, and the other is directed to the target surface where it is reflected (Fig. 2). If the target is moving in-line with the beam, the reflected light is Doppler shifted relative to the incident beam by

$$\Delta f = f_r - f_i = \frac{2v}{\lambda_i}, \tag{1}$$

where $f_r$ and $f_i$ are the frequencies of the reflected and incident beams, respectively, $v$ is the surface velocity component parallel with the incident beam, and $\lambda_i$ is the wavelength of the incident laser beam [11,33]. As shown in Fig. 2, the LDV measures the frequency of the reflected beam by recording the light intensity of the interference

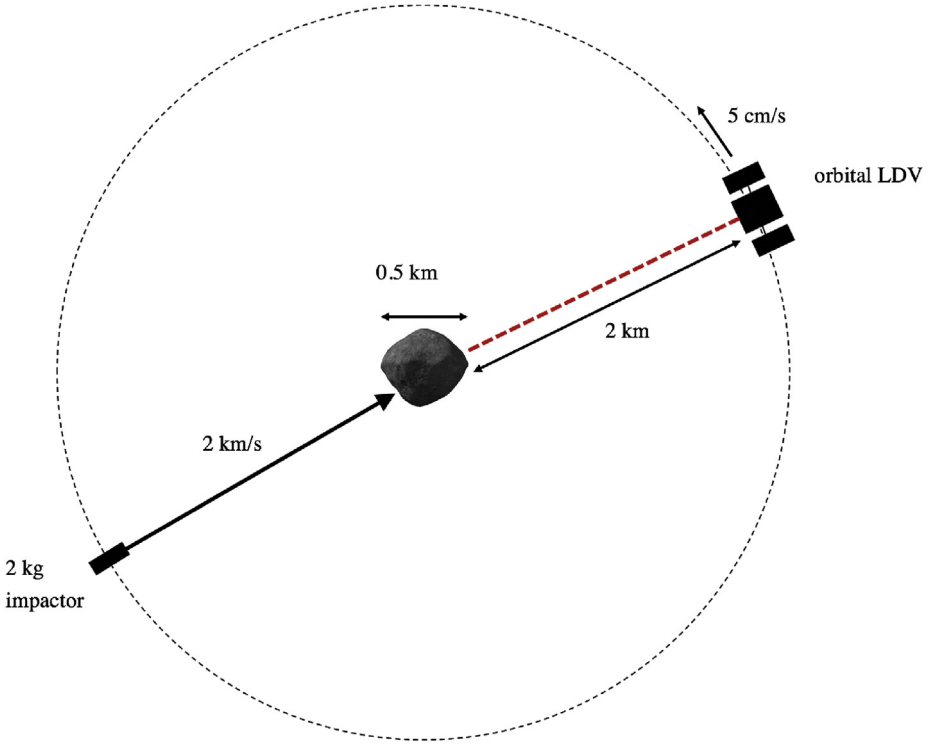


**Fig. 1.** The seismic data acquisition scenario. We simulate an LDV orbiting with a velocity of 2.5 cm/s at a distance of 2 km from the surface of 0.5 km wide asteroid 101955 Bennu. The impactor weighs 2 kg and travels at 2 km/s upon impact with the surface.

between the reference and reflected beam, a method known as optical heterodyning. As derived in Donges and Noll [33] and Sava and Asphaug [11], the light intensity recorded at the LDV's detector is a function of the surface velocity,

$$I(t) = I_r + I_i + 2\sqrt{I_r I_i}\cos\left[2\pi \int \left(\frac{2v(t)}{\lambda_i} + f_0\right)dt + (\varphi_i - \varphi_r)\right], \quad (2)$$

where $\varphi_i$ and $\varphi_r$ are the starting phases of the incident and reflected beams respectively, and $f_0$ is a known frequency shift applied to the reference beam through a Bragg cell [33]. The integral accounts for the accumulated phase shift in the reflected light as the surface moves with velocity $v$. As a whole, Equation (2) describes a frequency modulated signal with a carrier frequency $f_0$ and a modulation given by Equation (1). To recover the velocity of the surface, one must demodulate the intensity signal with the known carrier frequency, $f_0$.

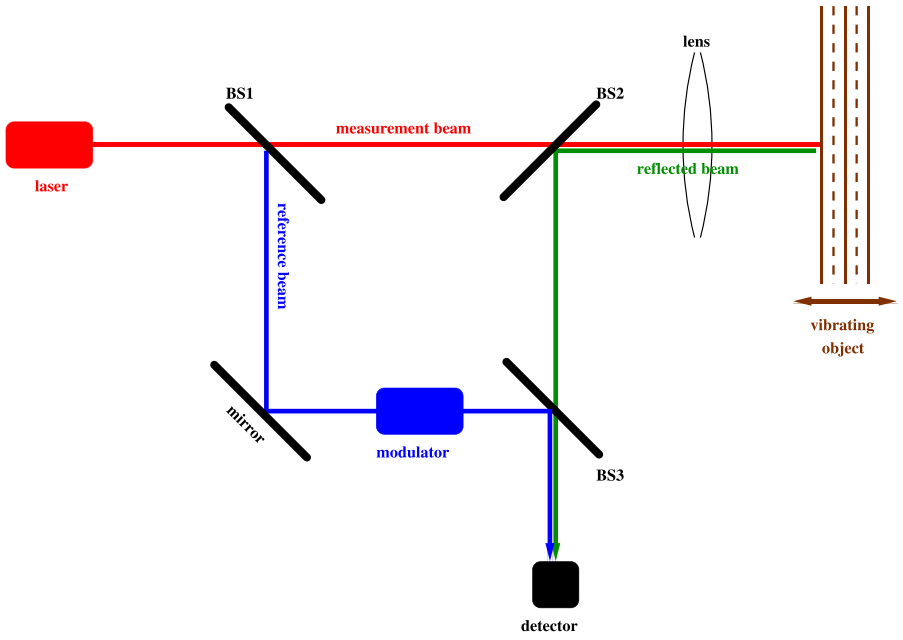


**Fig. 2.** A schematic of a Laser Doppler Vibrometer (LDV). The original laser beam is split into a measurement and reference beam at the first beam splitter (BS1). The measurement beam is directed at a vibrating target. In-line motion of the target Doppler shifts the frequency of the reflected beam. Upon return, the reflected beam is redirected by BS2 toward the detector. BS3 combines the reflected and reference beams. Due to the frequency shift of the reflected beam, the combined beams produce time dependent interference (optical heterodyning), which contains information about the surface motion (Equation (2)).

### 2.2. Laser speckle patterns

Equation (2) assumes that the target behaves like a mirror, where the light is reflected specularly and remains spatially coherent over the size of the LDV's detector. Light is said to be spatially coherent if each location in the light's wavefront has the same phase [34]. Any spatial incoherence in the reflected wavefront can reduce the power and accuracy of the resulting LDV velocity measurement. To behave like a mirror, an object must have surface roughness that is less than the wavelength of the incident light [27]. In this paper, we quantify the surface roughness as the root mean square (RMS) deviation from the average surface height. We classify a rough surface as one with roughness greater than 775 nm, which is the wavelength of the laser considered in this study. After reflection from such a rough surface, laser light becomes spatially incoherent because the rough surface acts as an incoherent source [27]. The Van Cittert-Zernike Theorem states that light from an incoherent source, such as the reflectance from a rough surface, only appears spatially coherent if the condition, $r \gg d^2/\lambda$, is satisfied, where $r$ is the distance to the surface, $d$ is the diameter of the detector, and $\lambda$ is the wavelength of the laser light [34]. This condition is not satisfied under our acquisition scenario where $r = 2$ km, $\lambda = 775$ nm, and $d$ is similar to typical LDV aperture sizes of a few centimeters [35]. Thus, if the asteroid's surface is rough, the reflected light returning to the detector is no longer spatially coherent. The spatial incoherence manifests as a laser speckle pattern [26], pictured in Fig. 3. The LDV detector samples a portion of the reflected speckle pattern.

To simulate a speckle pattern, we approximate a rough surface as a collection of Lambertian tiles. Constructive and destructive interference at the detector from ray paths originating at tiles with different path

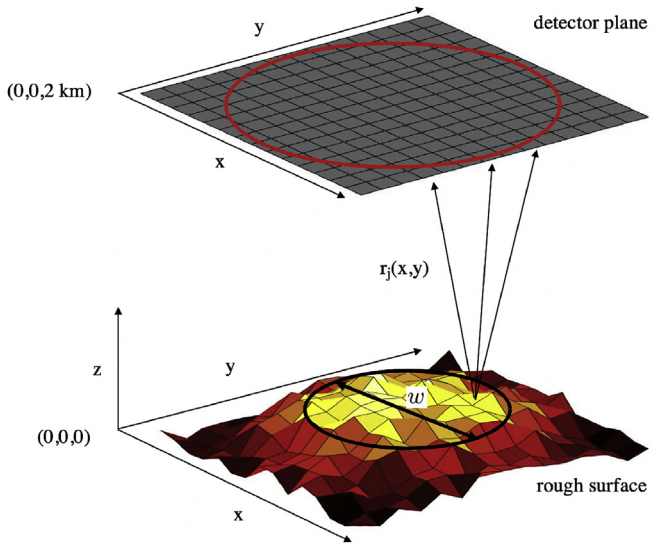


**Fig. 4.** Illustration of speckle pattern computation from a rough surface (not to scale). Each surface tile contributes to the electric field recorded at the detector plane. The detector plane is 2 km above the rough surface. The red circle indicates the area of the LDV detector. The black circle with diameter $w$ indicates the $1/e^2$ Gaussian beam footprint. (For interpretation of the references to color in this figure legend, the reader is referred to the Web version of this article.)

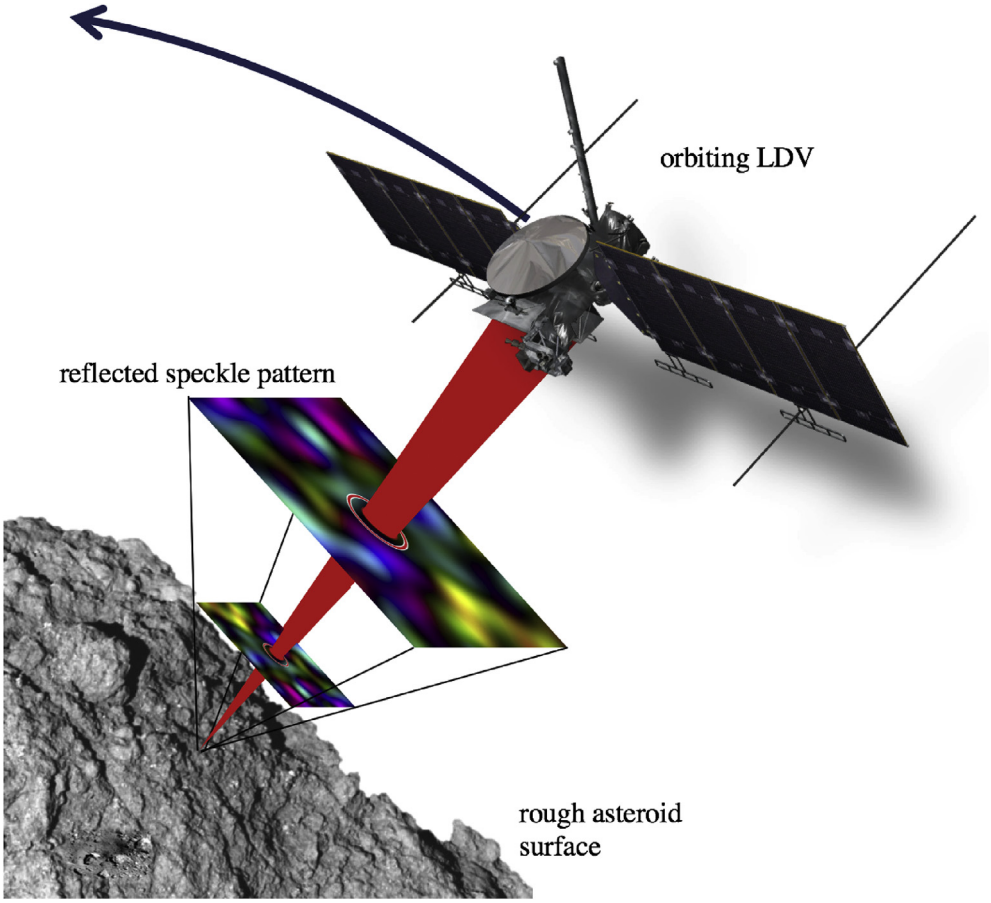


**Fig. 3.** Illustration of how a coherent laser beam is reflected as an incoherent speckle pattern if the surface is rough. Not to scale; the beam and speckle sizes are exaggerated.

lengths, as a result of surface roughness, produces a speckle pattern. The reflected electric field from the $j^{th}$ tile observed at a location $(x, y)$ on a detector plane located a distance $z$ above the target surface is

$$\mathbf{E}_j(x, y) = C_j(x, y)\hat{\mathbf{E}}_0 e^{i(kr_j(x,y)+2\pi ft+\varphi_i)}, \tag{3}$$

where $\hat{\mathbf{E}}_0$ denotes the unit vector polarization of the starting laser beam (we assume linear polarization), $k$ denotes the laser wavenumber, $r_j(x, y)$ is the distance between the $j^{th}$ surface tile and the $(x, y)$ location on the detector plane, $f$ is the frequency of light, $\varphi_i$ is the initial phase of the incident beam, and $C_j$ is a scaling factor (Fig. 4). This model does not consider multiple scattering, and thus the reflected light retains the same polarization as the incident beam. In reality, reflected laser light from a scattering surface may become de-polarized [36]. For our purpose, this can be effectively approximated by assigning a random polarization vector to each tile. Since light is a transverse wave and the LDV is positioned kilometers away from a centimeter scale laser spot, the z component of the polarization is many orders of magnitude less than the polarization in x or y, and can be ignored. The scaling factor

$$C_j(x, y) = \left(\frac{\alpha_j}{2\pi\,(r_j(x, y))^2}\right)\left(\frac{2P_0}{\pi w^2}\right)e^{-2\frac{d_j^2}{w^2}}, \tag{4}$$

accounts for the percent amplitude of light reflected by the $j^{th}$ tile with albedo $\alpha_j$, the spherical geometrical spreading, and the power of the incident beam's Gaussian profile. The variable $w$ is the $1/e^2$ beam diameter,[1] $d_j$ is the $j^{th}$ tile's distance from the center of the beam profile, and $P_0$ is the incident beam peak power. Since we are only interested in the relative phases from each tile, we can ignore the time dependency and assume $\varphi_i = 0$, thus simplifying Equation (3) to,

$$\mathbf{E}_j(x, y) = C_j(x, y)\hat{\mathbf{E}}_0 e^{ikr_j(x,y)}. \tag{5}$$

The total electric field at each detector point $(x, y)$ is given by the sum of the electric fields from all $n$ surface tiles,

$$\mathbf{E}(x, y) = \sum_{j=1}^{n} \mathbf{E}_j(x, y). \tag{6}$$

The intensity of light at each detector location is given by,

$$I(x, y) = \frac{c\varepsilon_0}{2}\left|\mathbf{E}(x, y)\right|^2, \tag{7}$$

and the phase by,

$$\varphi(x, y) = \tan^{-1}\left(\frac{\mathrm{Im}(\mathbf{E}(x, y))}{\mathrm{Re}(\mathbf{E}(x, y))}\right), \tag{8}$$

where $c$ is the speed of light and $\varepsilon_0$ is the vacuum permittivity.

Using Equations (7) and (8), we simulate speckle patterns from surfaces in different surface roughness regimes. Fig. 5 illustrates that speckle patterns only develop when the surface roughness is greater than the light's wavelength. As mentioned previously, If the surface has roughness less than the wavelength of light, the surface acts like a mirror. We also generate speckle patterns from surfaces with similar surface roughness (RMS height variation), but with different lateral roughness (distance between topographic high points). Fig. 6 shows that the size and intensity of the speckles remain similar for surfaces with different lateral heterogeneity. This observation agrees with Drabenstedt [27] and Guo et al. [37], who show that, counter-intuitively, speckle pattern statistical properties are independent of the surface roughness properties, provided the roughness is greater than the light wavelength. In general, the mean speckle diameter, $d_s$, is given by,

$$d_s = \frac{2\lambda_i r}{\pi w} \tag{9}$$

where $\lambda_i$ is the laser wavelength, $r$ is the distance to the target surface, and $w$ is the $1/e^2$ diameter of the laser beam on the target surface [27]. For our study, we consider an LDV with a $1/e^2$ laser beam radius of 2.5 cm on the surface, which is consistent with existing long range LDVs [35]. In order to isolate the effect of laser speckle, we assume that there is no noise from background light, electrical components in the LDV, optical imperfections in the instrument, fluctuations in the LDV output laser beam, or instability of the spacecraft (jitter).

Do we expect rough surfaces on asteroids and comet surfaces? All current observations of small bodies say, "yes." From the first Hayabusa mission, it is known that 25143 Itokawa is largely composed of grains greater than 1 mm in size, with the spacecraft returning some grains with diameters on the order of 10s of microns back to Earth [38]. Observations from Hayabusa 2 show a similar story for 162173 Ryugu, where the smallest grain size appears to be on the order of 1–10 mm [39]. The recent arrival of OSIRIS-REx at asteroid 101955 Bennu has revealed that its surface is even coarser, dominated by pebbles with cm scale roughness [40]. Thermal inertia and polarimetry studies of larger asteroids, like 4 Vesta, show that smaller grains on the order of 10s of microns could be present [41,42]. Although it might be postulated that specular reflections could be present on comets with high ice content, the dust analyzer on the Rosetta spacecraft measured grains with sizes from 100s of μm to mm in size, and demonstrated that the comet was more dusty than icy. Thus, we assume that all known asteroid and comet surfaces exhibit surface roughness that is greater than the LDV wavelength. An exception may be the metallic surface of an asteroid like 16 Psyche [43], though this is highly speculative.

We acknowledge that asteroids often exhibit non-Lambertian surfaces that vary significantly in albedo. Although these photometric properties dictate the maximum light intensity expected to return to an orbiting LDV, they do not affect the size or distribution characteristics of the returning light's speckle pattern (c.f. Equation (9)). Thus, we do not expect a significant difference in speckle noise for a dark asteroid, such as Bennu, or a bright one. Future work analyzing the engineering requirements for the light detectors' sensitivity would require a more rigorous treatment of photometric properties, but that is outside the scope of this paper. For the purpose of analyzing speckle noise, our approximate approach is sufficient.

### 2.3. Speckle induced measurement error

When a stationary LDV points at a rough surface, speckle patterns are not a significant concern. If the detector happens to record a dark speckle location, the operator can simply re-aim the LDV until a bright speckle is sampled. However, if the observed speckle pattern changes with time, it is challenging to ensure a bright speckle would be sampled at all times. An evolving speckle pattern causes velocity measurement errors and signal dropouts as bright and dark speckles of the reflected light move over the detector.

Intuitively, the magnitude and frequency of the speckle noise depends on the speed at which an LDV moves relative to the surface. The faster the LDV spot moves across the surface, the faster the speckle pattern changes. We can quantify the noise affecting an orbital LDV based on the expected orbital velocity of a spacecraft relative to an asteroid. Fig. 7(b) illustrates a simulated velocity measurement as an LDV moves laterally at 5 cm/s over a motionless surface shown in Fig. 7(a). Note that the LDV records vertical velocity even though it should record no motion since the surface is static. The noise is uncorrelated with the surface profile. The only location where the noise subsides is at the location where the surface roughness drops below the wavelength of the laser light. This agrees with the literature that demonstrates speckle patterns to be independent from local surface properties, provided roughness is present [27,37].

[1] The $1/e^2$ radius of a laser beam with a Gaussian profile is the distance from the center of the laser beam to the point at which the intensity of the beam falls to $1/e^2$ (≈0.135) of the peak intensity of the beam.

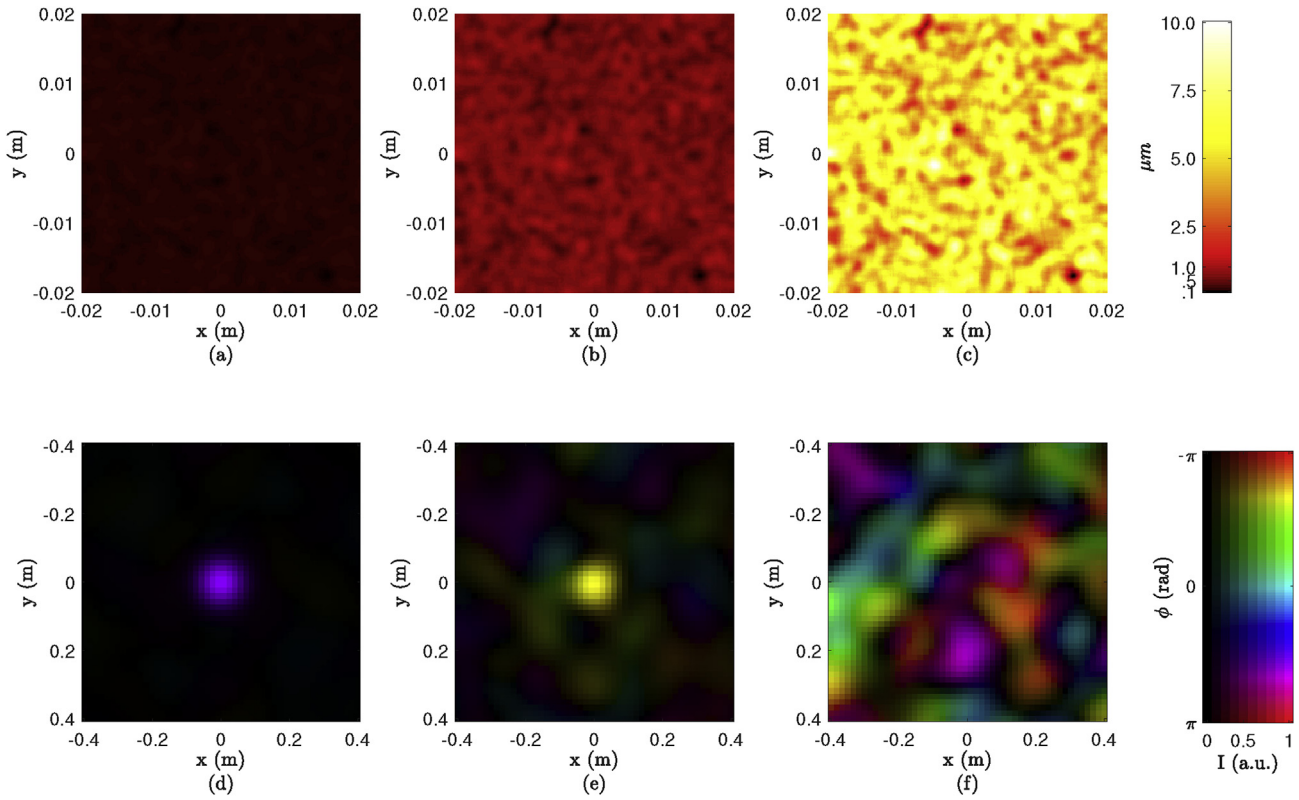


**Fig. 5.** Panels (a), (b), and (c) show random rough surfaces with peak relief of $10^{-7}$, $10^{-6}$, and $10^{-5}$ meters, respectively. Panels (d), (e), and (f), display the reflected light recorded at a detector 2 km away for the corresponding surfaces (a), (b), and (c). The simulated laser has a Gaussian beam profile with a $1/e^2$ radius of 2.5 cm, and a wavelength of 775 nm. When the surface roughness is less than wavelength (a), the surface acts as a mirror, and the beam profile is simply reflected (d). When the surface roughness is on the same order of magnitude as the laser wavelength (b), the reflected light has a bright center and a faint interference speckle pattern around it (e). For roughness much greater than the wavelength (c), a full speckle interference pattern develops (f).

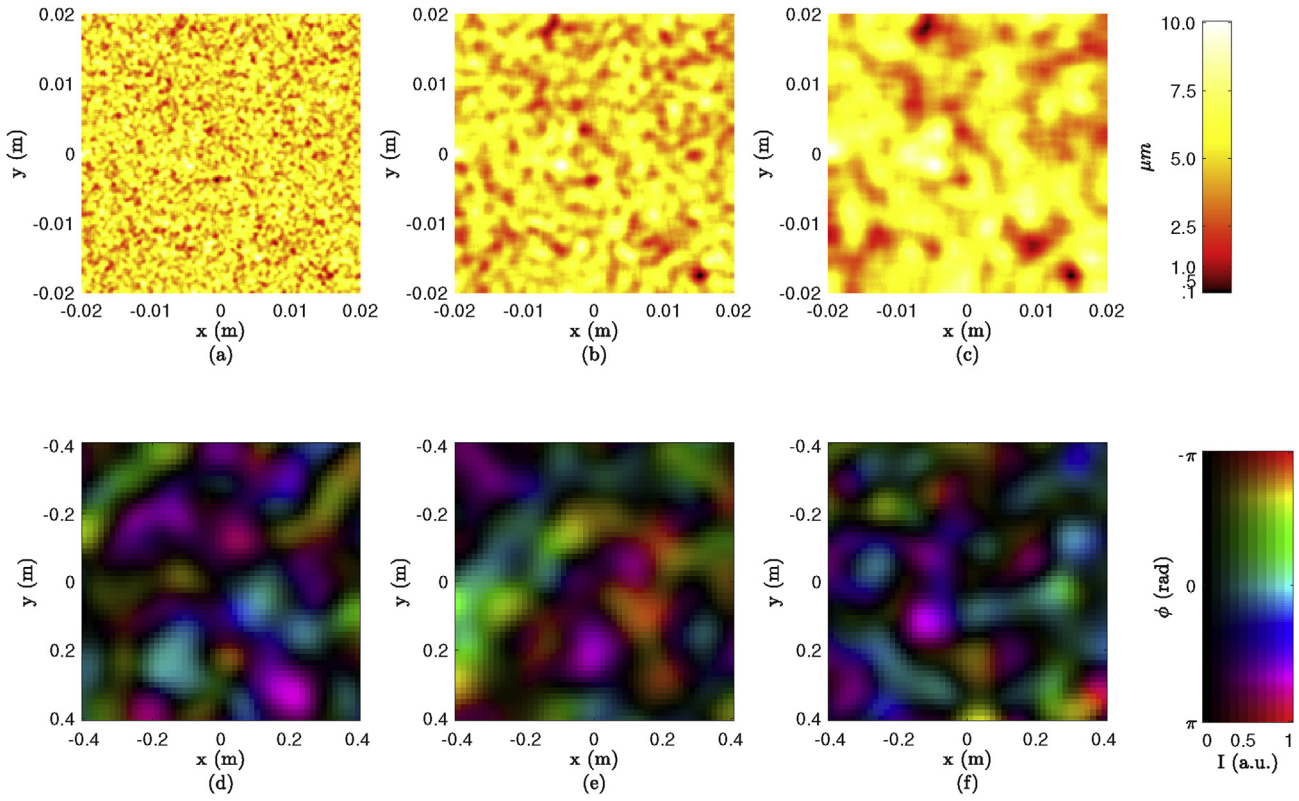


**Fig. 6.** Illustration of the property that speckle patterns are independent of the lateral roughness scale. The speckle pattern (d) from a rough surface with grains that are approximately 0.5 mm across (a) is statistically indistinct from speckle patterns (e) and (f), which were produced by grains that are 1 mm (b) or 5 mm across (c).

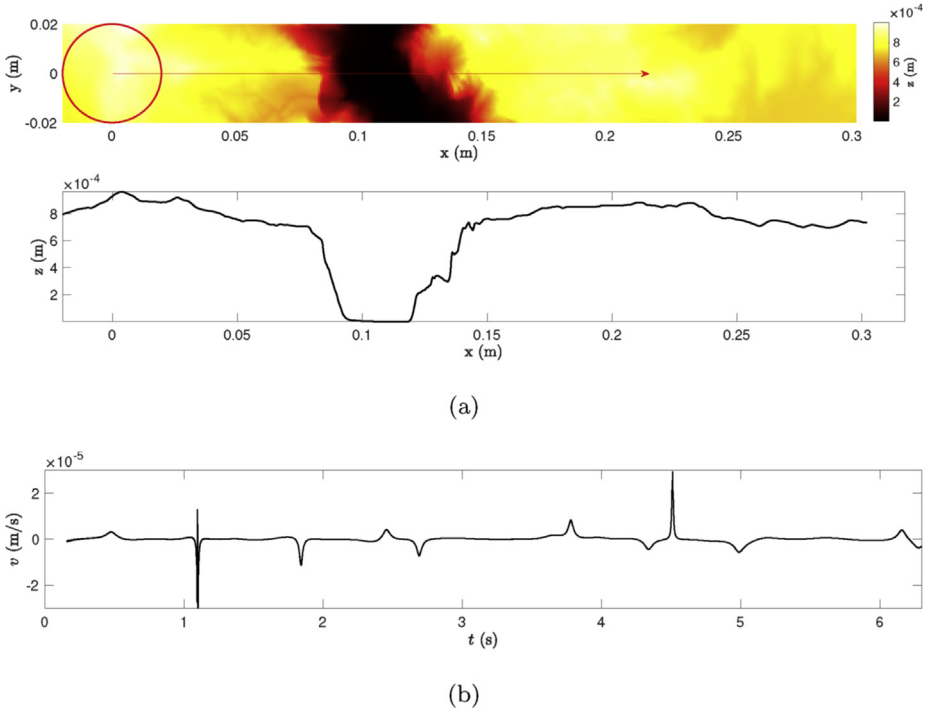


**Fig. 7.** (a) An example of rough topography (map and profile view) with multiple different scales of roughness. We simulate an LDV velocity measurement from a distance of 2 km as the laser spot moves across the map from left to right at a velocity of 5 cm/s. The red circle on the map view indicates the $1/e^2$ radius of the Gaussian laser spot. The surface is motionless. (b) Erroneous LDV velocity measurement from surface roughness induced speckle noise. (For interpretation of the references to color in this figure legend, the reader is referred to the Web version of this article.)

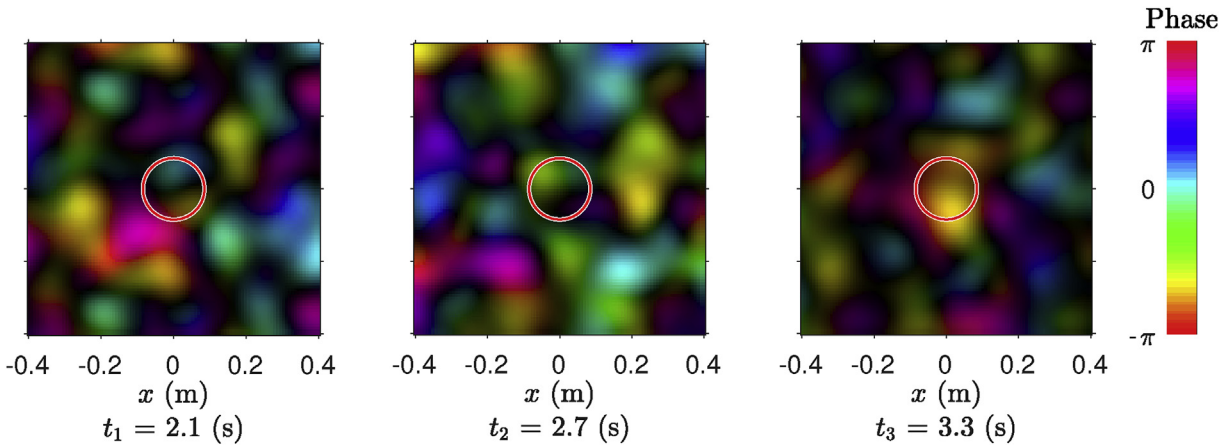


**Fig. 8.** Speckle patterns for the case when the laser spot moves across a rough surface at 5 cm/sec. The red circle indicates the detector size. $t_1$, $t_2$, and $t_3$ correspond to times when the detector records a dark, medium, and bright portion of the speckle pattern. (For interpretation of the references to color in this figure legend, the reader is referred to the Web version of this article.)

To better understand how speckle noise occurs, Fig. 8 illustrates three time steps of an evolving speckle pattern as a laser beam moves at 5 cm/s across a stationary surface. As the speckle pattern changes, the intensity and the phase recorded by the detector changes. Fig. 9 tracks the change in intensity and phase as a function of time as the laser spot moves across the rough surface. The phase changes most rapidly when the intensity is low. When the intensity is near zero, it only takes the contribution of one new surface tile to change the phase. When the intensity is high, many surface tiles are already in phase with each other, and one new surface tile cannot disrupt this coherence. Since the surface is stationary in this simulation, the LDV should record a constant zero velocity. However, because changing phase from an evolving speckle pattern appears the same as a frequency change, the LDV interprets it as a Doppler shift, and records an erroneous surface velocity. The velocity error is largest when the phase changes most rapidly, and the phase changes most rapidly when the intensity is low. The noise is characterized by smooth oscillations with occasional large spikes. The magnitude and frequency of the speckle noise becomes larger the faster the orbital velocity. By visual inspection of Fig. 9, it is apparent that intensity is a proxy for the variance of the speckle noise, as also demonstrated theoretically by Drbenstedt [44].

Using the acquisition scenario outlined in Fig. 1 and 10 shows three realizations of plausible speckle noise. This noise is inherent in the physics of an LDV operating on a rough surface. The large noise spikes occur randomly, and it is unlikely for large spikes to occur at the same time between multiple concurrent measurements.

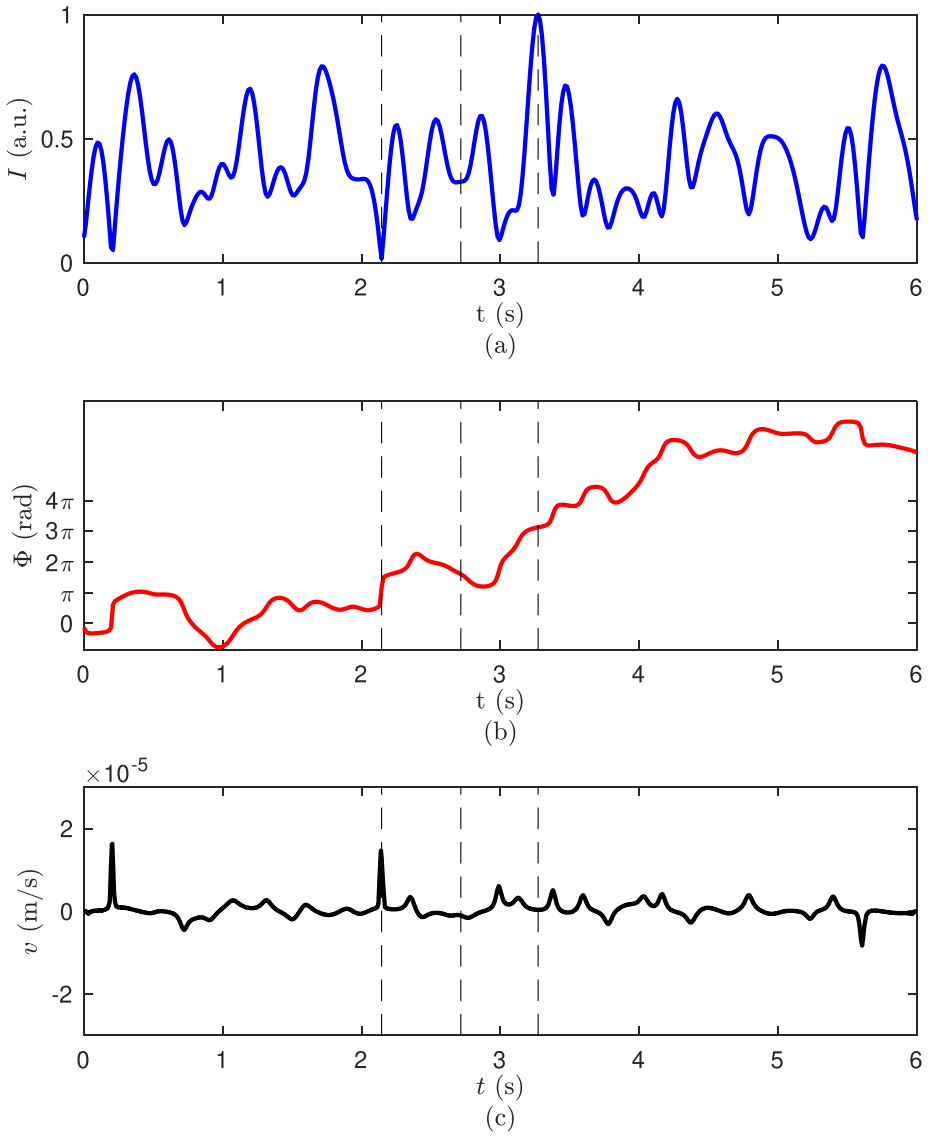


**Fig. 9.** (a) Illustration of LDV intensity recorded as a function of time, (b) the relative phase as a function of time, and (c) the erroneous velocity recorded by the LDV due to the variable phase. The dashed lines correspond to $t_1$, $t_2$, and $t_3$ in the speckle images in Fig. 8. The velocity signal has peaks when the phase changes quickly; the phase changes the quickest when the signal intensity is low.

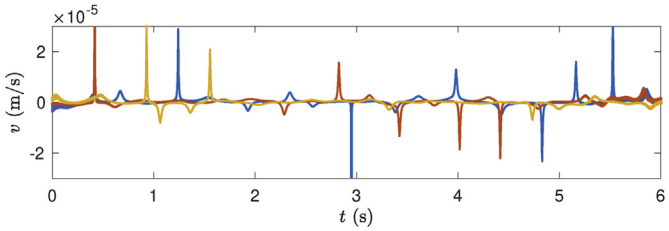


**Fig. 10.** Each different color curve corresponds to a realization of LDV speckle noise from an orbital LDV placed at 2 km from the surface and orbiting at 5 cm/s as depicted in Fig. 1. (For interpretation of the references to color in this figure legend, the reader is referred to the Web version of this article.)

### 2.4. Speckle noise reduction

We propose two ways to reduce speckle noise: (1) accurate spacecraft control, and (2) signal processing algorithms. For the first strategy, we suggest that the orbital LDV should be operated to minimize the motion of the laser spot on the surface. Designing the LDV so it can target a fixed point during a measurement could reduce speckle noise, albeit not eliminate it completely. An evolving speckle pattern would still occur because the detector plane moves relative to individual scattering points on the surface as the spacecraft rotates to aim the laser spot at the same ground location. Fig. 11 illustrates that the RMS speckle noise scales linearly with orbital velocity in either the translational or rotational cases; however, the slope for the rotational case is significantly smaller. For the remainder of our paper, we assume a worst case scenario, in which the spacecraft makes no attempt to point at the same surface location.

Alternative to physically reducing speckle noise through spacecraft operation, we consider signal processing algorithms. The seismic signal and the speckle noise can be separated by taking advantage of the different properties of the signal and noise. The remainder of this paper outlines how to describe impact-induced seismic signals and how to separate seismic signals from speckle noise based on their attributes.

## 3. Impact seismic signal simulation

### 3.1. Impact source

To properly consider how to separate speckle noise from seismic

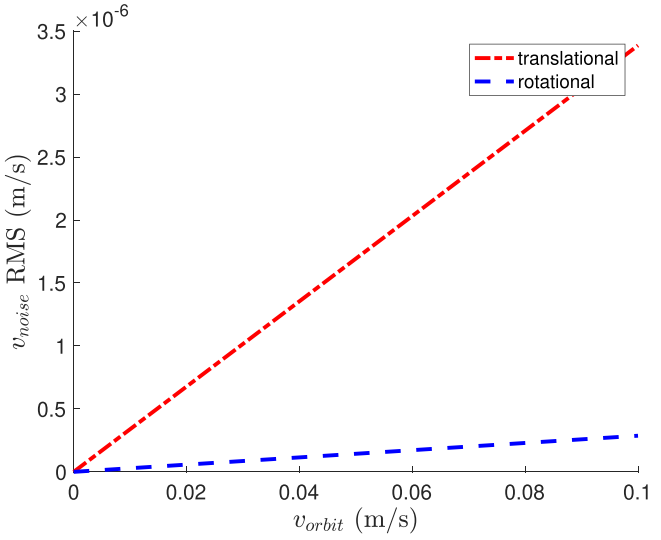


**Fig. 11.** Simulated RMS velocity noise as a function of orbital velocity for an LDV positioned 2 km from an asteroid surface. The LDV has a 775 nm laser with a $1/e^2$ spot radius of 2.5 cm. The speckle noise is larger if the beam translates over the asteroid surface (red) than in the case where the beam rotates about a fixed point on the surface (blue). (For interpretation of the references to color in this figure legend, the reader is referred to the Web version of this article.)

signals, we need a model of the ground motion signal as a function of time. We consider an impact source for two reasons: 1) natural impacts have occurred on asteroids, and several studies suggest that they can induce global surface shaking at the asteroid surface [17,45]; and 2) synthetic impacts on small body surfaces have been demonstrated by past space missions, e.g. Deep Impact and Hayabusa2 [31,46]. For the purpose of our study, we use Hayabusa2's Small Carry-on Impactor (SCI) as the seismic source model. The SCI had a mass of 2 kg and was accelerated to a velocity of 2 km/s, yielding a nominal 8 MJ of kinetic energy upon impact [31]. Since an impactor like SCI would be small relative to seismic wavelengths, we approximate it as a point source.

Following Meschede et al. [47], we describe an impact point force as,

$$\mathbf{f}(\mathbf{x}, t) = \hat{\mathbf{f}}\, p\, S(t)\delta(\mathbf{x} - \mathbf{x}_s), \tag{10}$$

where $p$ is the momentum of the impacting object, $S(t)$ is the source time function, $\delta$ is the delta function locating the impact at point $\mathbf{x}_s$, and $\hat{\mathbf{f}}$ is the direction of the impact relative to the surface normal. As suggested by Meschede et al. [47], we assume that the source time function is a Gaussian,

$$S(t) = \sqrt{\frac{\pi}{\tau^2}}\, e^{\frac{-\pi^2 t^2}{\tau^2}}, \tag{11}$$

where $\tau$ is the halfwidth of the seismic pulse. For such Gaussian source time functions, the seismic energy is,

$$E_s(t) = \frac{F^2\pi^{3/2}}{2^{5/2}\tau^3\rho}\left(\frac{1}{3v_p^3} + \frac{2}{3v_s^3}\right), \tag{12}$$

where $F$ is the momentum of the impactor, $v_p$ and $v_s$ are the longitudinal and transverse wave velocities of the medium, respectively, and ρ is the density of the target surface [30].

The time constant, $\tau$, is not well constrained [47]. We can estimate $\tau$ based on the seismic efficiency of the impact, $k$, which is defined as the ratio of kinetic energy transferred into seismic energy upon impact [47],

$$k = \frac{E_s}{E_k}. \tag{13}$$

Laboratory testing indicates that large impacts in weak materials can have a seismic efficiency as little as $k \approx 10^{-5}$ [48], whereas smaller well coupled impacts or buried explosions can have a much higher seismic efficiency of up to $k \approx 10^{-2}$ [49,50]. More recent studies combining laboratory measurements and numerical simulations suggest that the seismic efficiency of impacts can be constrained between $k \approx 10^{-5}$ and $k \approx 10^{-3}$ [51,52]. We use these values as low and high bounds for the seismic energy expected from an impactor. By estimating the seismic energy in Equation (13) from the seismic efficiency and the impactor's kinetic energy, we can solve for $\tau$ using Equation (12), and then use Equation (11) to describe the source pulse.

We assume that the instrument records seismic signals on the opposite side of its target body for two reasons: 1) the instrument would record waves that travel through the center of the asteroid, and 2) the spacecraft would be safe from any debris from the impact. If we assume that the asteroid is a homogeneous medium, the vertical surface displacement from a longitudinal wave recorded on the opposite side of 101955 Bennu from an impact is

$$u^p(t) = \frac{1}{4\pi d_B \rho v_p^2} S\left(t - \frac{d_B}{v_p}\right), \tag{14}$$

where $d_B$ is the diameter of 101955 Bennu, and $S$ is the source time function, Equation (11) [30]. By taking the derivative of Equation (14), we get the velocity of the surface at the LDV measurement location.

For an impactor analogous to Hayabusa2's SCI, we find seismic energy concentrated between 5 and 200 Hz. Significant uncertainty characterizes the seismic efficiency of an impact in asteroid regolith, so the ranges in the expected frequency and peak ground velocity (PGV) are large. Fig. 12 illustrates a synthetic seismogram for an ideal impact source after propagating 500 m, about the diameter of 101955 Bennu, in a homogeneous medium with $v_p = 450$ m/s. This velocity is consistent with estimated seismic velocities in the near surface lunar regolith [53,54]. For a high seismic efficiency case of $k = 10^{-3}$, a peak frequency of 60 Hz would be expected and a PGV of 0.1 mm/s would be possible. For the low seismic efficiency case of $k = 10^{-5}$, a peak frequency of 20 Hz would be expected and a PGV of 5 μm/s would be possible. In general, a smaller seismic efficiency leads to a lower amplitude and frequency, and a higher seismic efficiency leads to a higher amplitude frequency. We evaluate the ability to separate speckle noise from seismic signals based on the worst case seismic efficiency, $k = 10^{-5}$.

### 3.2. Seismic propagation through 101955 Bennu

Fig. 12 provides an estimate of the peak ground velocity and frequency content due to an impact source, but does not adequately capture the complexity of true seismic signals. It is unlikely that a small asteroid like 101955 Bennu behaves as a homogeneous medium. The best interpretations from the OSIRIS-REx mission suggest that 101955 Bennu is a rubble pile [6], likely dominated by boulders that are on the order of tens of meters in diameter [55], which is similar to typical seismic wavelengths. For scenarios where heterogeneities in the medium are on the same scale as seismic wavelengths, scattering theory or numerical simulations are necessary to create synthetic seismograms [30].

Fig. 13 illustrates a conceptual rubble pile asteroid velocity model, consisting of angular blocks that represent impact shards that have gravitationally fallen together, as described by Asphaug [18] and Scheeres et al. [2]. We assume that no large void spaces are present, or that they have been filled with regolith, which acts as a low seismic velocity medium. The compressional seismic wave velocity of asteroid materials is unknown; however, asteroid regolith likely has a similar velocity to regolith on the Moon. The near lunar surface exhibits a compressional wave velocity of around 300 m/s and gradually increases with depth [53,54]. Per contra, laboratory measurements of carbonaceous meteorites suggest that intact asteroid fragments could

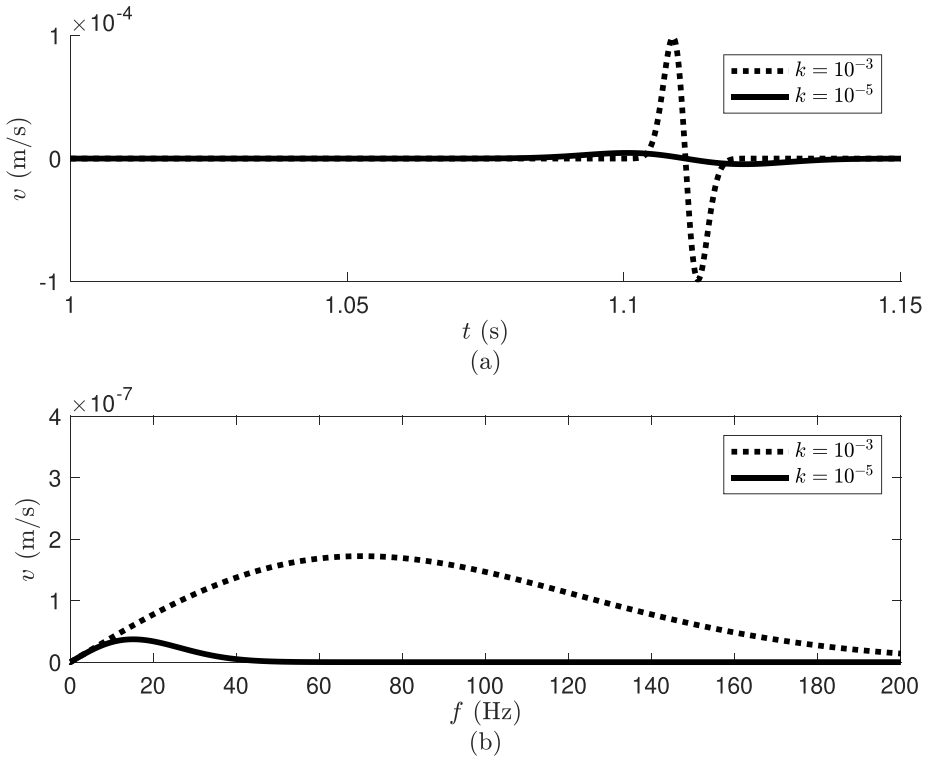


**Fig. 12.** (a) The ground motion signals from an impact seismic source similar to the Hayabusa2 SCI after propagating 500 m in a 450 m/s velocity homogeneous model. The examples shown correspond to high efficiency $k = 10^{-3}$ and low efficiency $k = 10^{-5}$ impacts. (b) Illustrates the frequency spectrum of the seismic signals.

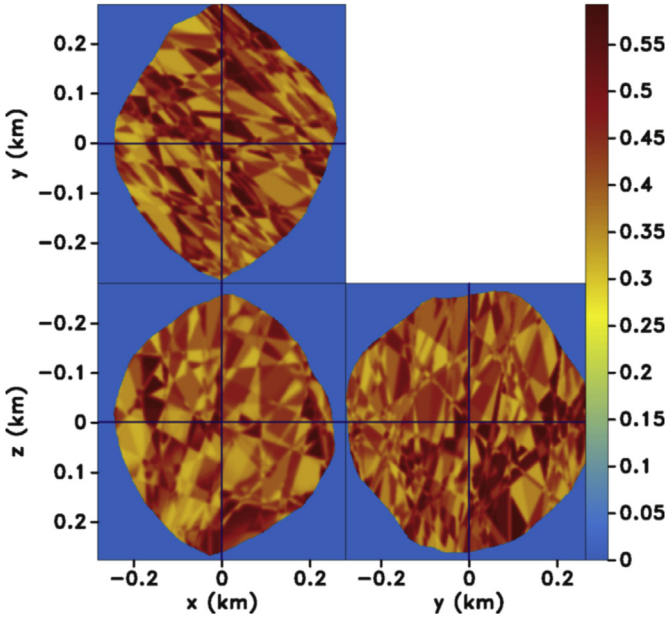


**Fig. 13.** Rubble pile asteroid velocity model we use to simulate seismic signals.

have velocities as fast as 1–6 km/s [56]. However, these measurements were made on centimeter sized samples with compressional waves in the MHz frequency range and may not be indicative of the bulk properties of asteroids at the seismic wavelength scale. The seismic velocity of lunar regolith is likely a better analog for asteroidal regolith because both are expected to contain brecciated or impact derived and gardened debris, meaning they likely share a common macro-scale structure. Thus, for our rubble pile model, we assume velocities between 300 m/s to 600 m/s, which is consistent with estimated velocities in the near lunar surface. We simulate compressional wave propagation through the model using acoustic finite differences to generate a synthetic seismogram at a location on the opposite side of the asteroid from of the impact source. We also scale the synthetic seismogram by an exponentially decaying curve to approximate intrinsic attenuation using a seismic quality factor of $Q = 3000$, which is consistent with the low intrinsic attenuation observed in the lunar crust [57].

Fig. 14 illustrates wavefield snapshots for a low seismic efficiency $k = 10^{-5}$ impact. The asteroid's heterogeneity leads to significant wavefield scattering within the interior of the body. Since the asteroid is surrounded by vacuum, the scattered waves cannot escape from the asteroid's interior, and continue to ring throughout the asteroid. Fig. 15 displays the resulting synthetic seismogram from the worst case seismic efficiency impact wavefield simulation (c.f. Fig. 14). The wavefield scattering induced by the model heterogeneity reduces the PGV at the recording location as compared to the homogeneous propagation waveforms shown in Fig. 12. The synthetic seismogram is consistent with other asteroid impact modeling studies [17], which predict waveforms dominated by long-ringing coda from scattering. Fig. 15 also compares the synthetic seismogram with a speckle noise realization. The seismogram has a lower magnitude than the speckle noise, and falls below the amplitude spectrum of the speckle noise at all frequencies. This is a challenging signal separation problem since the noise has more power than the signal. We seek methods that attenuate the speckle noise, while boosting the power of the seismic signal. To address the seismic signal and speckle noise separation problem, we average multiple signals as suggested by Drbenstedt [44]. To further reduce speckle noise, we exploit the separation of the seismic signal from speckle noise in the frequency domain.

## 4. Seismic signal separation from speckle noise

### 4.1. Signal diversity

The ratio of seismic signal power to speckle noise power can be increased through signal diversity combining. Diversity combining

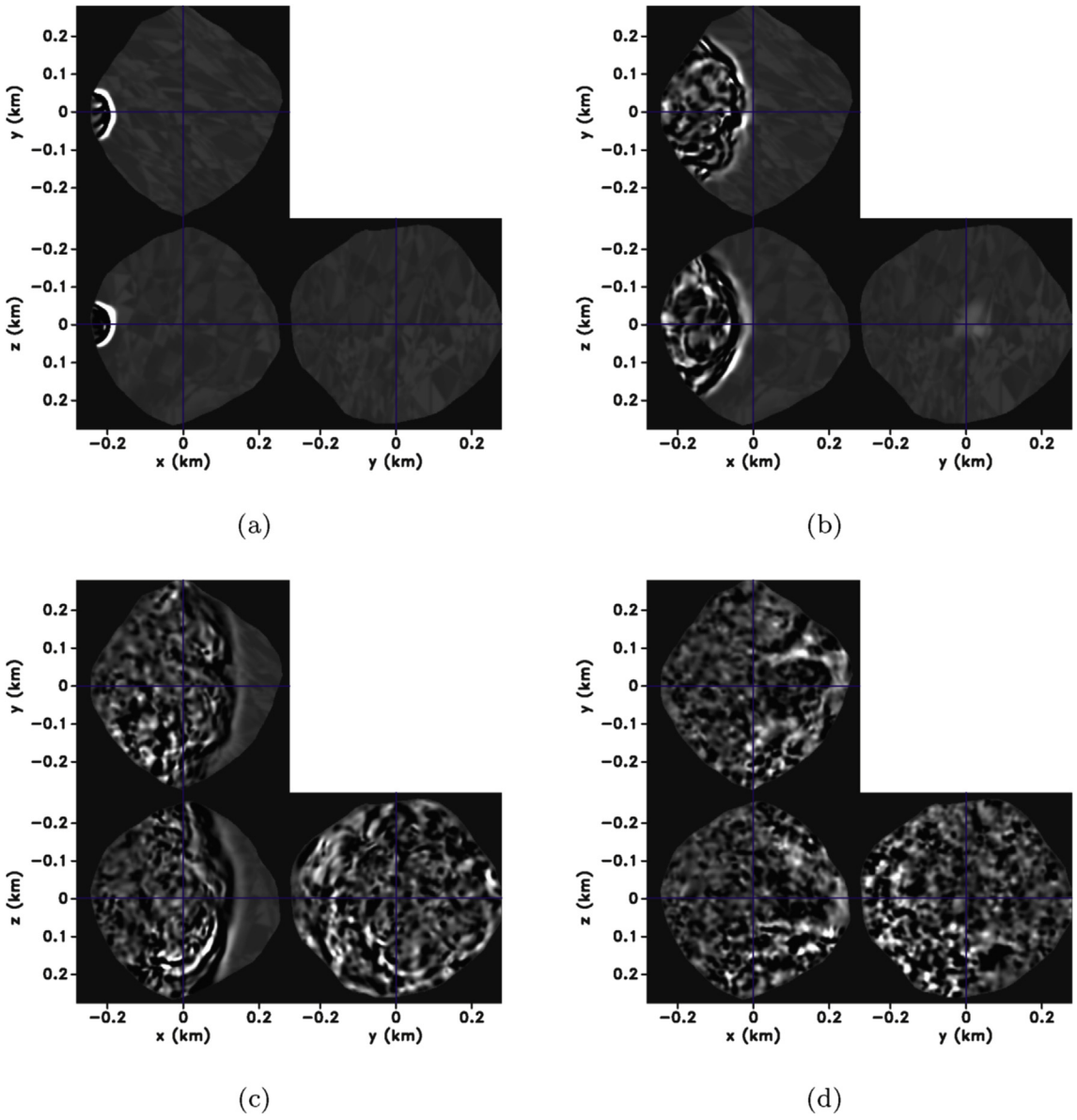


**Fig. 14.** Wavefield snapshots from an impactor with an efficiency of $10^{-5}$ at $t = 0.15$ s, $t = 0.45$ s, $t = 0.75$ s, and $t = 1.05$ s after impact, respectively. The impact occurs at $(-0.238,0,0)$ and the LDV makes a recording at $(0.240,0,0)$.

involves recording multiple measurements of the same signal and combining them to reduce the incoherent noise while boosting the coherent signal. This technique relies on the fact that all measurements record independent speckle noise, but have the same underlying ground velocity signal. Since all light in the speckle pattern originates from the same laser spot point on the surface (c.f. Fig. 3), any sampled portion of the speckle pattern would contain the same seismic signal. Thus, a single LDV can record multiple simultaneous ground velocity measurements by sampling multiple portions of the speckle pattern. Specifically, multiple detectors can exploit polarization and/or spatial diversity in the reflected speckle pattern [44,58]. Polarization diversity refers to the fact that orthogonal polarizations of the speckle pattern are independent. Thus, an LDV with two co-located detectors that record orthogonal polarization of light could record two simultaneous measurements that have independent speckle noise. Co-located means that the detectors sample light from the same spatial location within the speckle pattern. Drbenstedt [44] and Rembe and Drbenstedt [59] have successfully exploited polarization diversity in order to combine two signals. In order to combine more than two simultaneous measurements, we propose exploiting spatial diversity using an LDV with multiple detectors at separate, but closely adjacent spatial locations in the reflec Fig. 16 illustrates potential multiple detector layout options that allow for different portions of the speckle pattern to be sampled. The speckle noise observed by any two detectors separated in space would be uncorrelated as long as the detector's centers are placed more than an average speckle diameter apart, as quantified in Equation (9) [26]. Thus, each detector would record the same ground velocity signal, but have different noise.

### 4.2. Maximal ratio combining

There are different ways to combine signals that contain a common signal, but have independent noise. Drbenstedt [44] and Rembe and Drbenstedt [59] demonstrate signal diversity combining of two LDV signals via Maximal Ratio Combining (MRC). This method takes a weighted average at each time step of the observations using weights that maximize the signal to noise ratio (SNR). Mathematically, the $i^{th}$ signal, $s_i$, can be expressed as,

$$s_i(t) = v(t) + n_i(t) \tag{15}$$

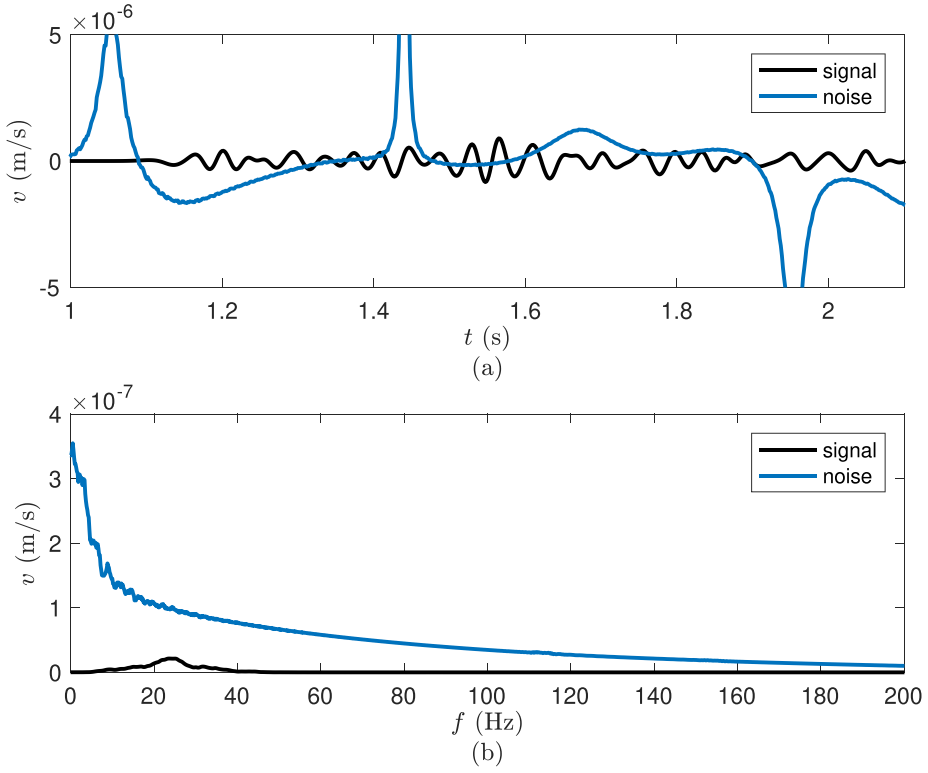


**Fig. 15.** Comparison of a speckle noise trace from Fig. 10 with a seismic trace from an impactor with a worst case efficiency of $k = 10^{-5}$. A low seismic efficiency impact produces a seismic signal with much lower amplitude than the speckle noise.

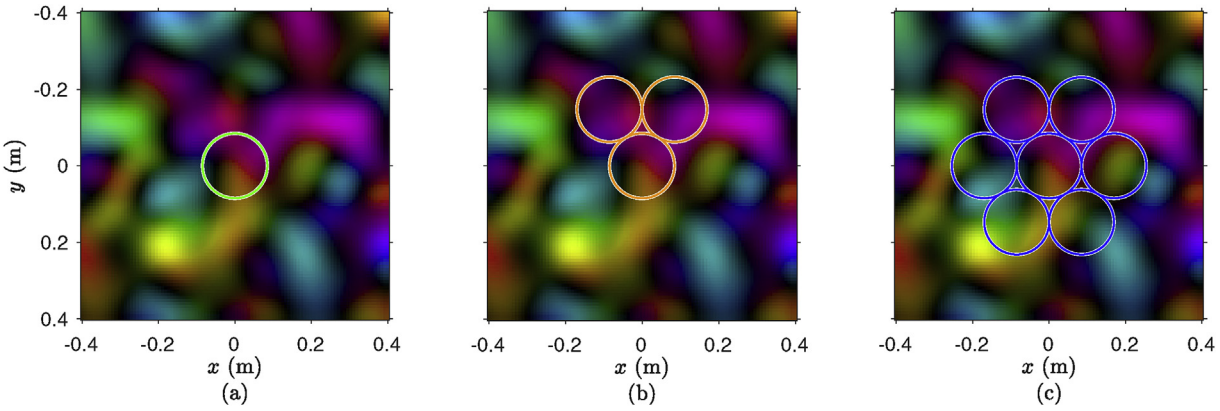


**Fig. 16.** LDV detector arrangements capable of recording multiple signals: (a) represents 1 detector recording 2 signals of orthogonal polarization, (b) 3 detectors recording 6 signals, and (c) 7 detectors recording 14 signals. Each detector is roughly the same size as the speckles in order to record independent speckle noise.

where $n_i(t)$ is the speckle noise unique for the $i^{th}$ detector, $v(t)$ is the surface velocity signal, and $t$ is time. Using the method described by Drbenstedt [44] and Rembe and Drbenstedt [59], an approximation of the ground velocity signal $\tilde{v}(t)$ can be achieved using a weighted sum of the signals,

$$\tilde{v}(t) = \sum_{i=1}^{n} w_i(t) s_i(t) \tag{16}$$

The weights $w$ should be chosen such that the variance of the resulting signal is minimized. Drbenstedt [44] demonstrates that the weights that satisfy this goal are given by

$$w_i(t) = \left[ \sum_{j=1}^{n} \frac{\sigma_i^2(t)}{\sigma_j^2(t)} \right]^{-1} \tag{17}$$

where $\sigma_i^2$ is the variance of the signal $\mathbf{s}_i$ from the ground velocity signal. The variance of each signal, $\sigma_i^2$, is unknown; however, Drbenstedt [44] shows that the variance of the speckle noise is inversely proportional to the total light intensity on the $i^{th}$ detector. Thus, the relative variance, $\sigma_i^2/\sigma_j^2$, between any two detectors with indices $i$ and $j$ is known. The relation between the velocity signal's variance and signal intensity is apparent in Fig. 9, where the large speckle noise spikes correlate with low signal intensity.

The weighted average solution in Equation (16) can be rewritten in matrix notation relating the signal from each LDV detector with the true ground velocity signal. Since we know that each signal recorded by a different detector has the same underlying ground velocity signal, we can write,

$$\mathbf{d} = \mathbf{I}\mathbf{v}, \tag{18}$$

where $\mathbf{v}$ is a column vector of the true ground velocity signal $v(t)$, $\mathbf{I}$ is an $M$-high stack of $N \times N$ identity matrices, and $\mathbf{d}$ is a column vector of the signal recorded by each detector stacked on top of each other,

$$\mathbf{d} = [\mathbf{s}_1\, \mathbf{s}_2 \ldots \mathbf{s}_M]^T. \tag{19}$$

In this formulation, $N$ is the length of each signal, $M$ is the number of detectors, and the vectors $\mathbf{s}_i$ represent time series of the velocity signals $s_i(t)$ recorded by each LDV detector. In the ideal case with no noise, as represented by Equation (18), each recorded signal vector $\mathbf{s}_i$ is a copy of the true ground motion signal vector, $\mathbf{v}$.

To solve for an approximation of the ground velocity $\tilde{\mathbf{v}}$ when given a data vector $\mathbf{d}$ contaminated with speckle noise, we solve a weighted least squares objective function,

$$\tilde{\mathbf{v}} = argmin_{\mathbf{v}} ||\mathbf{W}(\mathbf{d} - \mathbf{I}\mathbf{v})||^2 \tag{20}$$

where $\mathbf{W}$ is the weighting matrix, given by a diagonalization of the weights from Equation (17). Explicitly,

$$\mathbf{W} = \text{diag}([w_{11}\, w_{12} \ldots w_{MN}]), \tag{21}$$

where $w_{ij}$ is the weight for the $i^{th}$ receiver at the $j^{th}$ time index.

Solving Equation (20) produces the same result as the weighted average solution in Equation (16). The benefit of the matrix formulation is that we can modify it in order to take advantage of the signal characteristics. The next section describes how we use this formulation to impose structure on the recovered signal by exploiting the separation of the seismic signal and the speckle noise in the frequency domain.

### 4.3. Signal fitting model

Fig. 15 suggests that the seismic signal is concentrated in a narrow bandwidth. Thus, we assume that the true ground velocity signal $\mathbf{v}$ can be expressed by a band-limited subspace model,

$$\mathbf{v} = \mathbf{S}\mathbf{m}, \tag{22}$$

where $\mathbf{S}$ is the operator matrix that transforms a set of band-limited subspace model coefficients, $\mathbf{m}$, into a time domain signal. In this case, $\mathbf{S}$ is a tall matrix, meaning that $\mathbf{m}$ has fewer coefficients than $\mathbf{v}$.

We use Discrete Prolate Spheroidal Sequences (DPSS) to create band-limited subspaces because the sequences provide an efficient basis for sampled band-limited signals [60]. For a given signal length of $N$ samples and a bandwidth of $\beta$ Hz, the first DPSS is the unique length $N$ sequence that has maximum energy concentration within the band $[-\beta/2, \beta/2]$. The second DPSS is the sequence that is most energy concentrated in that band while also being orthogonal to the first vector. The third DPSS is the next most concentrated sequence in the band while being orthogonal to both the first and second sequences, and so on. Given a sampling frequency of $F_s$, the first $NF_s\beta - 1$ DPSS vectors have near complete energy concentration within the band $[-\beta/2, \beta/2]$. Any sequences after the $NF_s\beta - 1$ sequence have near zero energy within the band $[-\beta/2, \beta/2]$. Thus, the first $NF_s\beta - 1$ DPSS vectors form an ideal basis for a band-limited subspace spanning $[-\beta/2, \beta/2]$. A full derivation of DPSSs can be found in Slepian and Pollak [61] and Landau and Pollak [62], and a more recent summary and application is available in Davenport and Wakin [60].

Since we can estimate the bandwidth of the expected seismic signal based on impactor modeling, we can estimate a center frequency $f_c$ and a bandwidth $\beta$ to construct a DPSS transform matrix. However, by definition, DPSSs are centered around zero frequency, such that the sequences provide support for all frequencies in the range $-\beta/2$ to $\beta/2$. To create a band-limited subspace centered around a frequency $f_c$, we modulate all sequences by $f_c$, as described in Davenport and Wakin [60],

$$\mathbf{S} = e^{i2\pi f_c t}\mathbf{S}_0, \tag{23}$$

where, $\mathbf{S}_0$ is the zero center set of DPSSs that satisfy the given bandwidth $\beta$. The result, $\mathbf{S}$, denotes the operator that transforms coefficients of band-limited DPSS vectors centered at a frequency $f_c$ to a time domain signal. Fig. 17 illustrates how well the seismic trace in Fig. 15 is approximated by different bandwidths. For example, an approximation of over 20 dB can be achieved with a subspace spanning a bandwidth of 50 Hz centered around 30 Hz.

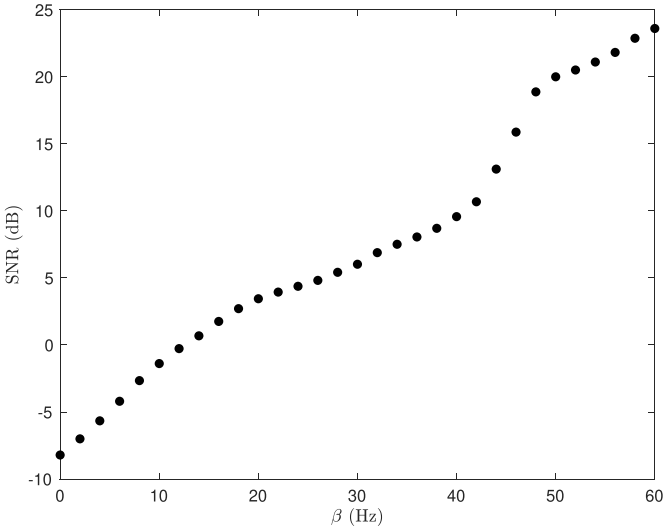


**Fig. 17.** Signal-to-noise ratio of a band-limited subspace approximation of the seismic trace in Fig. 15 as a function of the subspace's bandwidth. The band is centered at 30 Hz, so a bandwidth of 15 Hz corresponds to a subspace that spans 15–45 Hz. The seismic signal can be well approximated using a narrow bandwidth.

As previously stated, each LDV detector records the same ground velocity. Thus, each signal should be related to the same band-limited subspace coefficients. Using this knowledge, we relate the recorded signals, $\mathbf{d}$, to a set of coefficients, $\mathbf{m}$, in the band-limited subspace with the operator $\mathbf{G}$,

$$\mathbf{d} = \mathbf{G}\mathbf{m}, \tag{24}$$

where $\mathbf{G}$ is an M-high stack of $\mathbf{S}$ matrices,

$$\mathbf{G} = [\mathbf{S}\mathbf{S}...\mathbf{S}]^T. \tag{25}$$

We solve a modified inverse problem by finding $\tilde{\mathbf{m}}$ such that,

$$\tilde{\mathbf{m}} = argmin_{\mathbf{m}} ||\mathbf{W}(\mathbf{d} - \mathbf{G}\mathbf{m})||^2 \tag{26}$$

Using conventional inverse theory, the weighted least squares solution to Equation (26) [63] is,

$$\tilde{\mathbf{m}} = (\mathbf{G}^\mathbf{T}\mathbf{W}^\mathbf{T}\mathbf{W}\mathbf{G})^{-1}\mathbf{G}^\mathbf{T}\mathbf{W}^\mathbf{T}\mathbf{W}\mathbf{d}, \tag{27}$$

where the weighting matrix is the same as Equation (21). Finally, the time domain seismic signal is recovered by,

$$\tilde{\mathbf{v}} = \mathbf{S}\tilde{\mathbf{m}}. \tag{28}$$

We note that the seismic impulses we consider are not perfectly band-limited. Thus, a band-limited subspace cannot fully recreate the seismic signal, as demonstrated in Fig. 17. In the imaginary scenario where we know the true seismic signal $\mathbf{v}$, we can find the optimal signal recovery by the projection of $\mathbf{v}$ onto the subspace spanned by $\mathbf{S}$. From Moon and Stirling [64], this is given by,

$$\tilde{\mathbf{v}}_{opt} = \mathbf{S}(\mathbf{S}^\mathbf{T}\mathbf{S})^{-1}(\mathbf{S}^\mathbf{T}\mathbf{v}). \tag{29}$$

The best SNR achievable using our algorithm is therefore the ratio of the power of $\mathbf{v}$ and $(\tilde{\mathbf{v}}_{opt} - \mathbf{v})$. Regardless of how many signals are combined, $\tilde{\mathbf{v}}$ will never provide a more accurate solution than $\tilde{\mathbf{v}}_{opt}$. Thus, the goal of our algorithm is to converge to $\tilde{\mathbf{v}}_{opt}$ with as few detectors as possible.

Fig. 18 illustrates the efficacy of our signal diversity combining algorithm by removing the speckle noise from the low efficiency impact seismic trace in Fig. 15 using a 7–53 Hz subspace approximation. An improvement of 10 dB to the SNR is achieved after combining two signals, and a further 10 dB is obtained upon combining 14 signals. Fig. 19 illustrates the SNR of the recovered signal in dB using our

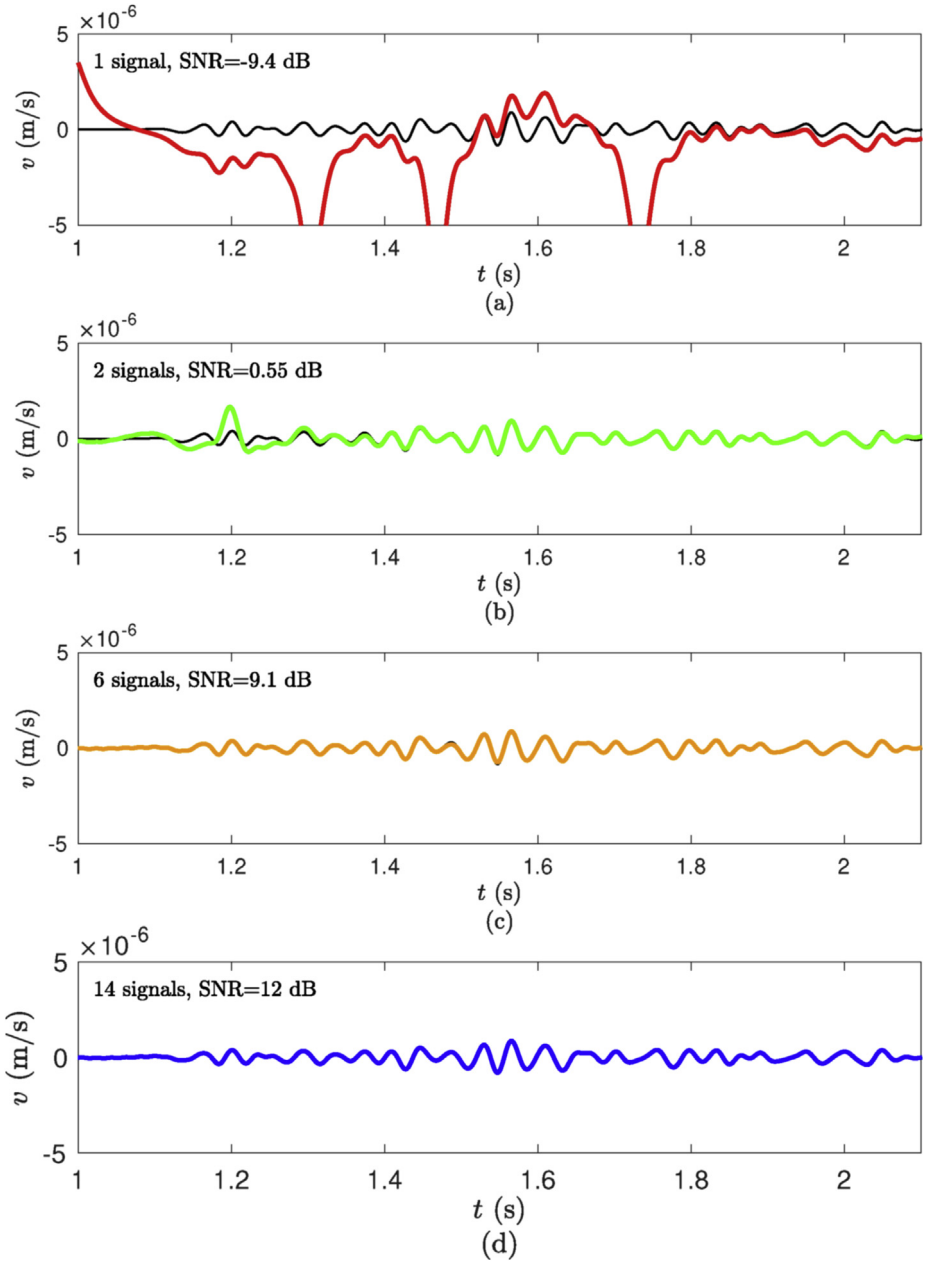


**Fig. 18.** Recovered signal after combining multiple data traces that contain the same seismic signal and similar speckle noise as in Fig. 15 (a) One LDV signal without any filtering; (b) combination two signals; (c) combination of six signals; (d) combination of 14 signals. Combining multiple signals significantly reduces speckle noise.

algorithm as a function of the number of independent signals recorded. The figure also shows the effect of using different bandwidths for signal separation. As more signals are added, the SNR approaches the ideal value, which is specific for each band-limited approximation. The more narrow the band, the lower the ideal approximation SNR, but the faster the convergence to that SNR. All band-limited cases achieve higher SNRs than the weighted average approach, as proposed by Ref. [44], provided an adequate bandwidth is chosen. Regardless of what combining method is used, there is diminishing return for each new signal combined. The combining of an additional signal does not guarantee SNR improvement because some speckle noise traces may have more large spikes over the time region of interest than others; however, on average the SNR improves with additional receivers. Fig. 19 illustrates SNR improvement curves from the average of 20 simulations. The uncertainty bars highlight the variability in improvement as a result of variability in the individual speckle noise traces.

Lastly, we demonstrate the recovery SNR as a function of PGV. The recovery of the seismic signal largely depends on the ratio in magnitude between the seismic signal and the speckle noise. To demonstrate how well we can separate the signals, we consider seismic signals with a range of PGV values. Using the seismogram from Fig. 15 with its PGV scaled with a range of values between $10^{-5}$ m/s and $10^{-8}$ m/s, we simulate separation from speckle noise. Fig. 20 illustrates that as the PGV increases, the recovery improves. We can push the possible signal recovery down to $10^{-8}$ m/s PGV with the inclusion of 14 detectors and our combining algorithm.

## 5. Discussion

Creating a detailed image of the interior of comets and asteroids is of high priority for the planetary science community [1,2,28]. To accomplish this, missions are routinely proposed using radar or seismic

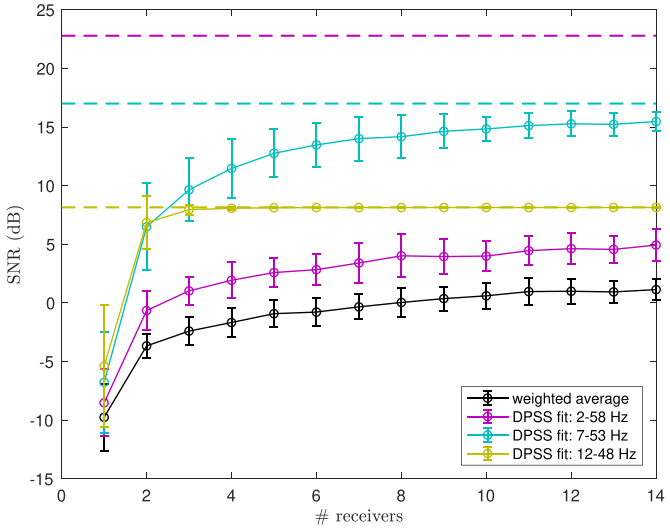


**Fig. 19.** Signal improvement as a function of the number of signals combined. Each curve indicates the average of 20 simulations, and the uncertainty bars represent the standard deviation of the simulations. Black illustrates the weighted average approach, yellow illustrates the case using a narrow band discrete prolate spheroidal sequence (DPSS) subspace to approximate the signal; magenta illustrates the case using a wide band for approximation, and cyan demonstrates a case using an optimal frequency band. (For interpretation of the references to color in this figure legend, the reader is referred to the Web version of this article.)

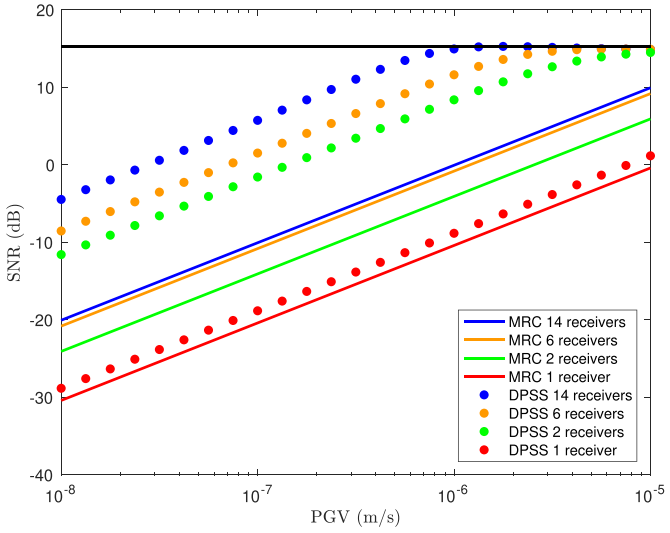


**Fig. 20.** Signal recovery as a function of the peak ground velocity of the seismic signal. The signal used for testing is the same as shown in Fig. 15, but scaled by different peak ground velocities ranging from $10^{-5}$ to $10^{-8}$ m/s. The dots indicate separation with a discrete prolate spheroidal sequence (DPSS) subspace fit within 7–53 Hz, and the lines indicate separation with the weighted average approach known as maximal ratio combining (MRC). Red represents the SNR from 1 receiver, green the SNR after combining 2 signals, yellow the SNR after combining 6 signals, and blue, the SNR after combining 14 signals. The black line indicates the optimal signal approximation using the chosen bandwidth. (For interpretation of the references to color in this figure legend, the reader is referred to the Web version of this article.)

theory to probe small body interiors [12,13,16,19]. However, radar imaging may only be viable in icy bodies that are nearly transparent to radar waves, and conventional seismic imaging may be prohibitively expensive and too technologically challenging to implement because multiple landed seismometers would be needed. The seismic imaging instrument concept proposed by Sava and Asphaug [11] seeks to alleviate these concerns by employing orbital LDVs as remote sensing seismometers. An orbital seismometer could obtain global seismic coverage of a small body and ultimately create a detailed image of its interior by using seismic migration and tomography techniques [11]. However, global seismic data coverage with an LDV is contingent on the LDV's ability to record seismic data anywhere on a rough asteroid surface. Our results provide support to the concept by demonstrating that we can separate surface roughness induced laser speckle noise from seismic signals recorded by an orbital laser Doppler vibrometer. By demonstrating that an LDV can theoretically record a seismic signal on a natural rough small body surface, our work supports the development of low-cost direct observations of small body interior properties via orbital laser Doppler vibrometry.

Following an orbital acquisition scenario at the asteroid 101955 Bennu (Fig. 1), we demonstrate in Fig. 20 that speckle noise is a minor issue for strong seismic shaking scenarios of more than $10^{-5}$ m/s PGV, and can be reduced through signal diversity combining for light seismic shaking scenarios of less than $10^{-5}$ m/s PGV. Our work shows that signal recovery can be achieved for signals with a PGV down to $10^{-8}$ m/s by assuming frequency bandwidth properties of the seismic signal, and combining multiple independent LDV measurements. In general, we demonstrate that the laser speckle noise observed by an LDV laser incident on a rough surface can be quantified and removed. Our simulation method allows for the speckle noise to be determined for any orbital acquisition scenario defined by orbital velocity, distance from surface, and laser properties (c.f. Fig. 11). We demonstrate that speckle noise can be combated with accurate spacecraft pointing, as demonstrated in Fig. 11, and by combining multiple LDV detectors, as demonstrated in Fig. 20. Thus, speckle noise attenuation in orbital vibrometry can be applied to other orbital scenarios provided a suitable balance of seismic source energy, spacecraft pointing, and number of LDV receivers is achieved.

## 6. Conclusion

In the broader effort to enable orbital seismology of small planetary bodies such as asteroids and comets, we demonstrate how to attenuate surface roughness induced laser speckle noise in laser Doppler vibrometer measurements. Specifically, we demonstrate: (1) how to quantify laser speckle noise in laser Doppler vibrometer measurements on distant rough surfaces, (2) how to quantify seismic signals from artificial impacts, and (3) how to separate seismic signals from speckle noise. We demonstrate these concepts with numerical simulations of an orbital LDV collecting seismic data transmitted through the asteroid 101955 Bennu from an artificial impact source; however, the methods we show apply for any LDV data acquisition on a rough surface. We demonstrate that laser speckle noise can be reduced in two ways, (1) accurate spacecraft pointing, and (2) through signal diversity combining. Our work shows that, even under worst case conditions, an accurate seismic signal can be recovered in spite of LDV speckle noise while in orbit over a rough asteroid or comet surface.

This result has broader implications for the future exploration of asteroid and comet interiors. Sava and Asphaug [11] demonstrate that orbital laser Doppler vibrometry is a promising technique to remotely record seismic measurements on an asteroid or comet in order to create a detailed image of its interior, assuming that an LDV can provide an accurate measurement of ground motion on an unprepared asteroid or comet surface. This work provides a fundamental stepping stone toward achieving seismic imaging of small bodies by demonstrating that we can separate surface roughness induced laser speckle noise from seismic signals in simulated orbital LDV measurements.

## Acknowledgments

This work was supported by the NASA Planetary Instrument Concepts for the Advancement of Solar System Observations (PICASSO)

program (NNH16ZDA001N). The Center for Wave Phenomena at Colorado School of Mines provided logistic and computational support. The reproducible numeric examples in this paper use the Madagascar open-source software package freely available from http://www.ahay.org [65].

## References


[1] E. Asphaug, Growth and evolution of asteroids, Annu. Rev. Earth Planet Sci. 37 (2009) 413–448, https://doi.org/10.1146/annurev.earth.36.031207.124214.

[2] D.J. Scheeres, D. Britt, B. Carry, K.A. Holsapple, Asteroid interiors and morphology, Asteroids IV, University of Arizona, Tuscon, 2015, pp. 745–766.

[3] E. Asphaug, E.V. Ryan, M.T. Zuber, Asteroid interiors, Asteroids III, University of Arizona, Tuscon, 2002, pp. 463–484.

[4] M.B. Syal, J.M. Owen, P.L. Miller, Deflection by kinetic impact: sensitivity to asteroid properties, Icarus 269 (2016) 50–61, https://doi.org/10.1016/j.icarus.2016.01.010.

[5] M.A. Barucci, E. Dotto, A.C. Levasseur-Regourd, Space missions to small bodies: asteroids and cometary nuclei, Astron. AstroPhys. Rev. 19 (2011) 48, https://doi.org/10.1007/s00159-011-0048-2.

[6] O.S. Barnouin, M.G. Daly, E.E. Palmer, R.W. Gaskell, J.R. Weirich, C.L. Johnson, M.M. Al Asad, J.H. Roberts, M.E. Perry, H.C.M. Susorney, R.T. Daly, E.B. Bierhaus, J.A. Seabrook, R.C. Espiritu, A.H. Nair, L. Nguyen, G.A. Neumann, C.M. Ernst, W.V. Boynton, M.C. Nolan, C.D. Adam, M.C. Moreau, B. Rizk, C.Y. Drouet DAubigny, K.J. Walsh, P. Michel, S.R. Schwartz, R.-L. Ballouz, E.M. Mazarico, D.J. Scheeres, J.W. McMahon, W.F. Bottke, S. Sugita, N. Hirata, N. Hirata, S.-i. Watanabe, K.N. Burke, D.N. DellaGiustina, C.A. Bennett, D.S. Lauretta, D.E. Highsmith, J. Small, D. Vokrouhlick, N.E. Bowles, E. Brown, K.L. Donaldson Hanna, T. Warren, C. Brunet, R.A. Chicoine, S. Desjardins, D. Gaudreau, T. Haltigin, S. Millington-Veloza, A. Rubi, J. Aponte, N. Gorius, A. Lunsford, B. Allen, J. Grindlay, D. Guevel, D. Hoak, J. Hong, D.L. Schrader, J. Bayron, O. Golubov, P. Snchez, J. Stromberg, M. Hirabayashi, C.M. Hartzell, S. Oliver, M. Rascon, A. Harch, J. Joseph, S. Squyres, D. Richardson, J.P. Emery, L. McGraw, R. Ghent, R.P. Binzel, M.M.A. Asad, C.L. Johnson, L. Philpott, H.C.M. Susorney, E.A. Cloutis, R.D. Hanna, H.C. Connolly, F. Ciceri, A.R. Hildebrand, E.-M. Ibrahim, L. Breitenfeld, T. Glotch, A.D. Rogers, B.E. Clark, S. Ferrone, C.A. Thomas, H. Campins, Y. Fernandez, W. Chang, A. Cheuvront, D. Trang, S. Tachibana, H. Yurimoto, J.R. Brucato, G. Poggiali, M. Pajola, E. Dotto, E.M. Epifani, M.K. Crombie, C. Lantz, M.R.M. Izawa, J. de Leon, J. Licandro, J.L.R. Garcia, S. Clemett, K. Thomas-Keprta, S. Van wal, M. Yoshikawa, J. Bellerose, S. Bhaskaran, C. Boyles, S.R. Chesley, C.M. Elder, D. Farnocchia, A. Harbison, B. Kennedy, A. Knight, N. Martinez-Vlasoff, N. Mastrodemos, T. McElrath, W. Owen, R. Park, B. Rush, L. Swanson, Y. Takahashi, D. Velez, K. Yetter, C. Thayer, C. Adam, P. Antreasian, J. Bauman, C. Bryan, B. Carcich, M. Corvin, J. Geeraert, J. Hoffman, J.M. Leonard, E. Lessac-Chenen, A. Levine, J. McAdams, L. McCarthy, D. Nelson, B. Page, J. Pelgrift, E. Sahr, K. Stakkestad, D. Stanbridge, D. Wibben, B. Williams, Shape of (101955) Bennu indicative of a rubble pile with internal stiffness, Nat. Geosci. 12 (2019) 247–252, https://doi.org/10.1038/s41561-019-0330-x.

[7] S. Watanabe, M. Hirabayashi, N. Hirata, N. Hirata, R. Noguchi, Y. Shimaki, H. Ikeda, E. Tatsumi, M. Yoshikawa, S. Kikuchi, H. Yabuta, T. Nakamura, S. Tachibana, Y. Ishihara, T. Morota, K. Kitazato, N. Sakatani, K. Matsumoto, K. Wada, H. Senshu, C. Honda, T. Michikami, H. Takeuchi, T. Kouyama, R. Honda, S. Kameda, T. Fuse, H. Miyamoto, G. Komatsu, S. Sugita, T. Okada, N. Namiki, M. Arakawa, M. Ishiguro, M. Abe, R. Gaskell, E. Palmer, O.S. Barnouin, P. Michel, A.S. French, J.W. McMahon, D.J. Scheeres, P.A. Abell, Y. Yamamoto, S. Tanaka, K. Shirai, M. Matsuoka, M. Yamada, Y. Yokota, H. Suzuki, K. Yoshioka, Y. Cho, S. Tanaka, N. Nishikawa, T. Sugiyama, H. Kikuchi, R. Hemmi, T. Yamaguchi, N. Ogawa, G. Ono, Y. Mimasu, K. Yoshikawa, T. Takahashi, Y. Takei, A. Fujii, C. Hirose, T. Iwata, M. Hayakawa, S. Hosoda, O. Mori, H. Sawada, T. Shimada, S. Soldini, H. Yano, R. Tsukizaki, M. Ozaki, Y. Iijima, K. Ogawa, M. Fujimoto, T.-M. Ho, A. Moussi, R. Jaumann, J.-P. Bibring, C. Krause, F. Terui, T. Saiki, S. Nakazawa, Y. Tsuda, Hayabusa2 arrives at the carbonaceous asteroid 162173 Ryugu—a spinning top–shaped rubble pile, Science 364 (2019) 268–272, https://doi.org/10.1126/science.aav8032.

[8] M. Massironi, M. Massironi, E. Simioni, F. Marzari, G. Cremonese, L. Giacomini, M. Pajola, L. Jorda, G. Naletto, S. Lowry, M.R. El-Maarry, F. Preusker, F. Scholten, H. Sierks, C. Barbieri, P. Lamy, R. Rodrigo, D. Koschny, H. Rickman, H.U. Keller, M.F. AHearn, J. Agarwal, A.-T. Auger, M.A. Barucci, J.-L. Bertaux, I. Bertini, S. Besse, D. Bodewits, C. Capanna, V. Da Deppo, B. Davidsson, S. Debei, M. De Cecco, F. Ferri, S. Fornasier, M. Fulle, R. Gaskell, O. Groussin, P.J. Gutirrez, C. Gttler, S.F. Hviid, W.-H. Ip, J. Knollenberg, G. Kovacs, R. Kramm, E. Khrt, M. Kppers, F. La Forgia, L.M. Lara, M. Lazzarin, Z.-Y. Lin, J.J. Lopez Moreno, S. Magrin, H. Michalik, S. Mottola, N. Oklay, A. Pommerol, N. Thomas, C. Tubiana, J.-B. Vincent, Two independent and primitive envelopes of the bilobate nucleus of comet 67P, Nature 526 (2015) 402, https://doi.org/10.1038/nature15511.

[9] V. Ciarletti, A. Herique, J. Lasue, A.-C. Levasseur-Regourd, D. Plettemeier, F. Lemmonier, C. Guiffaut, P. Pasquero, W. Kofman, CONSERT constrains the internal structure of 67P at a few metres size scale, Mon. Not. Roy. Astron. Soc. 469 (2017) S805–S817, https://doi.org/10.1093/mnras/stx3132.

[10] A. Herique, B. Agnus, E. Asphaug, A. Barucci, P. Beck, J. Bellerose, J. Biele, L. Bonal, P. Bousquet, L. Bruzzone, C. Buck, I. Carnelli, A. Cheng, V. Ciarletti, M. Delbo, J. Du, X. Du, C. Eyraud, W. Fa, J.G. Fernandez, O. Gassot, R. Granados-Alfaro, S. Green, B. Grieger, J. Grundmann, J. Grygorczuk, R. Hahnel, E. Heggy, T.-M. Ho, O. Karatekin, Y. Kasaba, T. Kobayashi, W. Kofman, C. Krause, A. Kumamoto, M. Kppers, M. Laabs, C. Lange, J. Lasue, A. Levasseur-Regourd, A. Mallet, P. Michel, S. Mottola, N. Murdoch, M. Mtze, J. Oberst, R. Orosei, D. Plettemeier, S. Rochat, R. RodriguezSuquet, Y. Rogez, P. Schaffer, C. Snodgrass, J.-C. Souyris, M. Tokarz, S. Ulamec, J.-E. Wahlund, S. Zine, Direct observations of asteroid interior and regolith structure: science measurement requirements, Adv. Space Res. 62 (2018) 2141–2162 https://doi.org/10.1016/j.asr.2017.10.020.

[11] P. Sava, E. Asphaug, Seismology on small planetary bodies by orbital laser Doppler vibrometry, Adv. Space Res. 64 (2019) 527–544, https://doi.org/10.1016/j.asr.2019.04.017.

[12] E. Asphaug, M. Belton, D. Bockelee-Morvan, S. Chesley, M. Delbo, T. Farnham, Y. Gim, R. Grimm, A. Herique, W. Kofman, J. Oberst, R. Orosei, S. Piqueux, J. Plaut, M. Robinson, P. Sava, E. Heggy, W. Kurth, D. Scheeres, B. Denevi, E. Turtle, P. Weissman, The comet radar explorer mission, AAS/Div. Planet. Sci. Meet. Abstract. 46 (209.07) (2014) 59.

[13] P. Sava, D. Ittharat, R. Grimm, D. Stillman, Radio reflection imaging of asteroid and comet interiors I: acquisition and imaging theory, Adv. Space Res. 55 (2015) 2149–2165, https://doi.org/10.1016/j.asr.2014.10.021.

[14] P. Sava, E. Asphaug, 3D radar wavefield migration of comet interiors, Adv. Space Res. 62 (2018) 1146–1164.

[15] P. Sava, E. Asphaug, 3D radar wavefield tomography of comet interiors, Adv. Space Res. 61 (2018) 2198–2213.

[16] R.E. Grimm, D.E. Stillman, P. Sava, D. Ittharat, Radio reflection imaging of asteroid and comet interiors II: results and recommendations, Adv. Space Res. 55 (2015) 2166–2176, https://doi.org/10.1016/j.asr.2015.01.038.

[17] J.E. Richardson, H.J. Melosh, R.J. Greenberg, D.P. O'Brien, The global effects of impact-induced seismic activity on fractured asteroid surface morphology, Icarus 179 (2005) 325–349, https://doi.org/10.1016/j.icarus.2005.07.005.

[18] E. Asphaug, Critical crater diameter and asteroid impact seismology, Meteoritics Planet Sci. 43 (2008) 1075–1084, https://doi.org/10.1111/j.1945-5100.2008.tb00694.x.

[19] J.B. Plescia, O. Barnouin, M. Paul, N. Schmerr, D.C. Richardon, H. Yu, W. Schlei, M. Ozmiek, F. Siddique, J.V. DeMartini, Apex: asteroid probe experiment mission, 49th Lunar and Planetary Science Conference Abstract #1999, 2018.

[20] P. Castellini, G. Revel, E. Tomasini, Laser Doppler vibrometry: a review of advances and applications, Shock Vib. Digest 30 (1998) 443–456.

[21] W.J. Staszewski, R. bin Jenal, A. Klepka, M. Szwedo, T. Uhl, A review of laser Doppler vibrometry for structural health monitoring applications, Structural Health Monitoring II, Volume 518 of Key Engineering Materials, Trans Tech Publications Ltd, 2012, pp. 1–15, , https://doi.org/10.4028/www.scientific.net/KEM.518.1.

[22] S. Rothberg, M. Allen, P. Castellini, D.D. Maio, J. Dirckx, D. Ewins, B. Halkon, P. Muyshondt, N. Paone, T. Ryan, H. Steger, E. Tomasini, S. Vanlanduit, J. Vignola, An international review of laser Doppler vibrometry: making light work of vibration measurement, Optic Laser. Eng. 99 (2017) 11–22.

[23] A. Drbenstedt, X. Cao, U. Polom, F. Ptzold, T. Zeller, P. Hecker, V. Seyfried, C. Rembe, Mobile seismic exploration, AIP Conference Proceedings, vol. 1740, 2016030001, , , https://doi.org/10.1063/1.4952659.

[24] B.J. Halkon, S.J. Rothberg, Towards laser Doppler vibrometry from unmanned aerial vehicles, J. Phys. Conf. 1149 (2018) 012022, , https://doi.org/10.1088/1742-6596/1149/1/012022.

[25] T. Rapstine, P. Sava, E. Arias, Airborne seismic data acquisition using stereo vision, J. Unmanned Veh. Syst. 6 (2018) 31–42, https://doi.org/10.1139/juvs-2017-0019.

[26] S. Rothberg, B.J. Halkon, Laser vibrometry meets laser speckle, Proc. SPIE 5503 (2004) 5503–5503 – 12, https://doi.org/10.1117/12.579760.

[27] A. Drabenstedt, Quantification of displacement and velocity noise in vibrometer measurements on transversely moving or rotating surfaces, Proc. SPIE 6616 (2007), https://doi.org/10.1117/12.726115.

[28] R. Binzel, A. Morbidelli, S. Merouane, F.E. DeMeo, M. Birlan, P. Vernazza, C.A. Thomas, A.S. Rivkin, S.J. Bus, A.T. Tokunaga, Earth encounters as the origin of fresh surfaces on near-earth asteroids, Nature 463 (2010) 331, https://doi.org/10.1038/nature08709.

[29] D.S. Lauretta, C.W. Hergenrother, S.R. Chesley, J.M. Leonard, J.Y. Pelgrift, C.D. Adam, M. Al Asad, P.G. Antreasian, R.-L. Ballouz, K.J. Becker, C.A. Bennett, B.J. Bos, W.F. Bottke, M. Brozović, H. Campins, H.C. Connolly, M.G. Daly, A.B. Davis, J. de León, D.N. DellaGiustina, C.Y. Drouet d'Aubigny, J.P. Dworkin, J.P. Emery, D. Farnocchia, D.P. Glavin, D.R. Golish, C.M. Hartzell, R.A. Jacobson, E.R. Jawin, P. Jenniskens, J.N. Kidd, E.J. Lessac-Chenen, J.-Y. Li, G. Libourel, J. Licandro, A.J. Liounis, C.K. Maleszewski, C. Manzoni, B. May, L.K. McCarthy, J.W. McMahon, P. Michel, J.L. Molaro, M.C. Moreau, D.S. Nelson, W.M. Owen, B. Rizk, H.L. Roper, B. Rozitis, E.M. Sahr, D.J. Scheeres, J.A. Seabrook, S.H. Selznick, Y. Takahashi, F. Thuillet, P. Tricarico, D. Vokrouhlický, C.W.V. Wolner, Episodes of particle ejection from the surface of the active asteroid (101955) Bennu, Science 366 (2019), https://doi.org/10.1126/science.aay3544.

[30] K. Aki, P.G. Richards, Quantitative Seismology, second ed., University Science Books, 2002.

[31] T. Saiki, H. Sawada, C. Okamoto, H. Yano, Y. Takagi, Y. Akahoshi, M. Yoshikawa, Small carry-on impactor of Hayabusa2 mission, Acta Astronaut. 84 (2013) 227–236, https://doi.org/10.1016/j.actaastro.2012.11.010.

[32] M.G. Daly, O.S. Barnouin, C. Dickinson, J. Seabrook, C.L. Johnson, G. Cunningham, T. Haltigin, D. Gaudreau, C. Brunet, I. Aslam, A. Taylor, E.B. Bierhaus, W. Boynton, M. Nolan, D.S. Lauretta, The OSIRIS-REx laser altimeter (OLA) investigation and instrument, Space Sci. Rev. 212 (2017) 899–924.

[33] A. Donges, R. Noll, Laser Doppler methods, Laser Measurement Technology, Springer, 2015, pp. 279–303.

[34] A.R. Thompson, J.M. Moran, G.W. Swenson, Van Cittert–Zernike Theorem, Spatial

Coherence, and Scattering, Springer International Publishing, Cham, 2017, pp. 767–786, https://doi.org/10.1007/978-3-319-44431-4_15.
[35] A. Drbenstedt, J. Sauer, C. Rembe, Remote-sensing vibrometry at 1550 nm wavelength, AIP Conference Proceedings, 1457 2012, pp. 113–121, , https://doi.org/10.1063/1.4730549.
[36] S.P. Morgan, M.E. Ridgway, Polarization properties of light backscattered from a two layer scattering medium, Optic Express 7 (2000) 395–402, https://doi.org/10.1364/OE.7.000395.
[37] G. Guo, S. Li, Q. Tan, Statistical properties of laser speckles generated from far rough surfaces, Int. J. Infrared Millimet. Waves 22 (2001) 1177–1191, https://doi.org/10.1023/A:1015015232213.
[38] M. Yoshikawa, J. Kawaguchi, A. Fujiwara, Hayabusa sample return mission, Asteroids IV, University of Arizona, Tuscon, 2015, pp. 397–418.
[39] M. Hamm, M. Grott, E. Khrt, I. Pelivan, J. Knollenberg, A method to derive surface thermophysical properties of asteroid (162173) Ryugu (1999JU3) from in-situ surface brightness temperature measurements, Planet. Space Sci. 159 (2018) 1–10, https://doi.org/10.1016/j.pss.2018.03.017.
[40] D.S. Lauretta, D.N. DellaGiustina, C.A. Bennett, D.R. Golish, K.J. Becker, S.S. Balram-Knutson, O.S. Barnouin, T.L. Becker, W.F. Bottke, W.V. Boynton, H. Campins, B.E. Clark, H.C. Connolly, C.Y. Drouet dAubigny, J.P. Dworkin, J.P. Emery, H.L. Enos, V.E. Hamilton, C.W. Hergenrother, E.S. Howell, M.R.M. Izawa, H.H. Kaplan, M.C. Nolan, B. Rizk, H.L. Roper, D.J. Scheeres, P.H. Smith, K.J. Walsh, C.W.V. Wolner, D.E. Highsmith, J. Small, D. Vokrouhlick, N.E. Bowles, E. Brown, K.L. Donaldson Hanna, T. Warren, C. Brunet, R.A. Chicoine, S. Desjardins, D. Gaudreau, T. Haltigin, S. Millington-Veloza, A. Rubi, J. Aponte, N. Gorius, A. Lunsford, B. Allen, J. Grindlay, D. Guevel, D. Hoak, J. Hong, D.L. Schrader, J. Bayron, O. Golubov, P. Snchez, J. Stromberg, M. Hirabayashi, C.M. Hartzell, S. Oliver, M. Rascon, A. Harch, J. Joseph, S. Squyres, D. Richardson, J.P. Emery, L. McGraw, R. Ghent, R.P. Binzel, M.M.A. Asad, C.L. Johnson, L. Philpott, H.C.M. Susorney, E.A. Cloutis, R.D. Hanna, H.C. Connolly, F. Ciceri, A.R. Hildebrand, E.-M. Ibrahim, L. Breitenfeld, T. Glotch, A.D. Rogers, B.E. Clark, S. Ferrone, C.A. Thomas, H. Campins, Y. Fernandez, W. Chang, A. Cheuvront, D. Trang, S. Tachibana, H. Yurimoto, J.R. Brucato, G. Poggiali, M. Pajola, E. Dotto, E.M. Epifani, M.K. Crombie, C. Lantz, M.R.M. Izawa, J. de Leon, J. Licandro, J.L.R. Garcia, S. Clemett, K. Thomas-Keprta, S. Van wal, M. Yoshikawa, J. Bellerose, S. Bhaskaran, C. Boyles, S.R. Chesley, C.M. Elder, D. Farnocchia, A. Harbison, B. Kennedy, A. Knight, N. Martinez-Vlasoff, N. Mastrodemos, T. McElrath, W. Owen, R. Park, B. Rush, L. Swanson, Y. Takahashi, D. Velez, K. Yetter, C. Thayer, C. Adam, P. Antreasian, J. Bauman, C. Bryan, B. Carcich, M. Corvin, J. Geeraert, J. Hoffman, J.M. Leonard, E. Lessac-Chenen, A. Levine, J. McAdams, L. McCarthy, D. Nelson, B. Page, J. Pelgrift, E. Sahr, K. Stakkestad, D. Stanbridge, D. Wibben, B. Williams, K. Williams, P. Wolff, P. Hayne, D. Kubitschek, M.A. Barucci, J.D.P. Deshapriya, S. Fornasier, M. Fulchignoni, P. Hasselmann, F. Merlin, A. Praet, E.B. Bierh, The unexpected surface of asteroid (101955) Bennu, Nature 568 (2019) 55–60, https://doi.org/10.1038/s41586-019-1033-6.
[41] M. Delbo, M. Mueller, J.P. Emery, B. Rozitis, M.T. Capria, Asteroid thermophysical modeling, Asteroids IV, University of Arizona, Tuscon, 2015, pp. 107–128.
[42] L.A.M. Benner, M.W. Busch, J.D. Giorgini, P.A. Taylor, J.-L. Margot, Asteroid polarimetry, Asteroids IV, University of Arizona, Tuscon, 2015, pp. 151–164.
[43] A. Matter, M. Delbo, B. Carry, S. Ligori, Evidence of a metal-rich surface for the asteroid (16) Psyche from interferometric observations in the thermal infrared, Icarus 226 (2013) 419–427, https://doi.org/10.1016/j.icarus.2013.06.004.
[44] A. Drbenstedt, Diversity combining in laser Doppler vibrometry for improved signal reliability, AIP Conf. Proc. vol. 1600, 2014, pp. 263–273, , https://doi.org/10.1063/1.4879592.
[45] A.C. Quillen, Y. Zhao, Y. Chen, P. Snchez, R.C. Nelson, S.R. Schwartz, Impact excitation of a seismic pulse and vibrational normal modes on asteroid Bennu and associated slumping of regolith, Icarus 319 (2019) 312–333, https://doi.org/10.1016/j.icarus.2018.09.032.
[46] M.F. A'Hearn, M.J.S. Belton, W.A. Delamere, J. Kissel, K.P. Klaasen, L.A. McFadden, K.J. Meech, H.J. Melosh, P.H. Schultz, J.M. Sunshine, P.C. Thomas, J. Veverka, D.K. Yeomans, M.W. Baca, I. Busko, C.J. Crockett, S.M. Collins, M. Desnoyer, C.A. Eberhardy, C.M. Ernst, T.L. Farnham, L. Feaga, O. Groussin, D. Hampton, S.I. Ipatov, J.-Y. Li, D. Lindler, C.M. Lisse, N. Mastrodemos, W.M. Owen, J.E. Richardson, D.D. Wellnitz, R.L. White, Deep impact: excavating comet tempel 1, Science 310 (2005) 258–264, https://doi.org/10.1126/science.1118923.
[47] M.A. Meschede, C.L. Myhrvold, J. Tromp, Antipodal focusing of seismic waves due to large meteorite impacts on Earth, Geophys. J. Int. 187 (2011) 529–537, https://doi.org/10.1111/j.1365-246X.2011.05170.x.
[48] H.J. Moore, G.V. Latham, W.G. Mcdonald, Missile inpacts as sources of seismic energy on the Moon, Science 168 (1970) 242–244, https://doi.org/10.1126/science.168.3928.242.
[49] D.E. Gault, The partition of energy for hypervelocity impact craters formed in rock, Proc. Sixth Hypervelocity Impact Symp. 2 (1963) 419–456.
[50] S.R. Titley, Seismic energy as an agent of morphologic modification on the moon, U.S. Geol. Survey, Astrogeologic Studies, Ann. Prog. Repr. pt. A (1966) 87–101.
[51] N. Güldemeister, K. Wünnemann, Quantitative analysis of impact-induced seismic signals by numerical modeling, Icarus 296 (2017) 15–27.
[52] K. Matsue, M. Yasui, M. Arakawa, S. Hasegawa, Measurements of seismic waves induced by high-velocity impacts: implications for seismic shaking surrounding impact craters on asteroids, Icarus (2019) 113520, https://doi.org/10.1016/j.icarus.2019.113520.
[53] R.L. Kovach, J.S. Watkins, The velocity structure of the lunar crust, Moon 7 (1973) 63–75, https://doi.org/10.1007/BF00578808.
[54] A. Heffels, M. Knapmeyer, J. Oberst, I. Haase, Re-evaluation of Apollo 17 lunar seismic profiling experiment data, Planet. Space Sci. 135 (2017) 43–54, https://doi.org/10.1016/j.pss.2016.11.007.
[55] D.N. DellaGiustina, J.P. Emery, D.R. Golish, B. Rozitis, C.A. Bennett, K.N. Burke, R.-L. Ballouz, K.J. Becker, P.R. Christensen, C.Y. Drouet dAubigny, V.E. Hamilton, D.C. Reuter, B. Rizk, A.A. Simon, E. Asphaug, J.L. Bandfield, O.S. Barnouin, M.A. Barucci, E.B. Bierhaus, R.P. Binzel, W.F. Bottke, N.E. Bowles, H. Campins, B.C. Clark, B.E. Clark, H.C. Connolly, M.G. Daly, J.d. Leon, M. Delbo, J.D.P. Deshapriya, C.M. Elder, S. Fornasier, C.W. Hergenrother, E.S. Howell, E.R. Jawin, H.H. Kaplan, T.R. Kareta, L. Le Corre, J.-Y. Li, J. Licandro, L.F. Lim, P. Michel, J. Molaro, M.C. Nolan, M. Pajola, M. Popescu, J.L.R. Garcia, A. Ryan, S.R. Schwartz, N. Shultz, M.A. Siegler, P.H. Smith, E. Tatsumi, C.A. Thomas, K.J. Walsh, C.W.V. Wolner, X.-D. Zou, D.S. Lauretta, D.E. Highsmith, J. Small, D. Vokrouhlick, N.E. Bowles, E. Brown, K.L. Donaldson Hanna, T. Warren, C. Brunet, R.A. Chicoine, S. Desjardins, D. Gaudreau, T. Haltigin, S. Millington-Veloza, A. Rubi, J. Aponte, N. Gorius, A. Lunsford, B. Allen, J. Grindlay, D. Guevel, D. Hoak, J. Hong, D.L. Schrader, J. Bayron, O. Golubov, P. Snchez, J. Stromberg, M. Hirabayashi, C.M. Hartzell, S. Oliver, M. Rascon, A. Harch, J. Joseph, S. Squyres, D. Richardson, J.P. Emery, L. McGraw, R. Ghent, R.P. Binzel, M.M.A. Asad, C.L. Johnson, L. Philpott, H.C.M. Susorney, E.A. Cloutis, R.D. Hanna, H.C. Connolly, F. Ciceri, A.R. Hildebrand, E.-M. Ibrahim, L. Breitenfeld, T. Glotch, A.D. Rogers, B.E. Clark, S. Ferrone, C.A. Thomas, H. Campins, Y. Fernandez, W. Chang, A. Cheuvront, D. Trang, S. Tachibana, H. Yurimoto, J.R. Brucato, G. Poggiali, M. Pajola, E. Dotto, E.M. Epifani, M.K. Crombie, C. Lantz, M.R.M. Izawa, J. de Leon, J. Licandro, J.L.R. Garcia, S. Clemett, K. Thomas-Keprta, S. Van wal, M. Yoshikawa, J. Bellerose, S. Bhaskaran, C. Boyles, S.R. Chesley, C.M. Elder, D. Farnocchia, A. Harbison, B. Kennedy, A. Knight, N. Martinez-Vlasoff, N. Mastrodemos, T. McElrath, W. Owen, R. Park, B. Rush, L. Swanson, Y. Takahashi, D. Velez, K. Yetter, C. Thayer, C. Adam, P. Antreasian, J. Bauman, C. Bryan, Properties of rubble-pile asteroid (101955) Bennu from OSIRIS-REx imaging and thermal analysis, Nature Astronomy 3 (2019) 341–351, https://doi.org/10.1038/s41550-019-0731-1.
[56] S. Jones, Elastic Wave Velocity, Porosity, and Pore Geometry of Ordinary Chondrites and Artificially Shocked Samples, Master's thesis, University of Calgary Department of Geosciences, 2009.
[57] Y. Nakamura, J. Koyama, Seismic Q of the lunar upper mantle, J. Geophys. Res.: Solid Earth 87 (1982) 4855–4861, https://doi.org/10.1029/JB087iB06p04855.
[58] M. Schussler, C. Rembe, A. Drabenstedt, S. Boedecker, T. Xu, Device and method for an interferometric measuring of an object, U.S. Patent 9 (Jan. 2017) 551–726.
[59] C. Rembe, A. Drbenstedt, Speckle-insensitive laser-Doppler vibrometry with adaptive optics and signal diversity, AMA Conf. Proc. (2015) 505–510, https://doi.org/10.5162/sensor2015/D1.1.
[60] M.A. Davenport, M.B. Wakin, Compressive sensing of analog signals using discrete prolate spheroidal sequences, Appl. Comput. Harmon. Anal. 33 (2012) 438–472, https://doi.org/10.1016/j.acha.2012.02.005.
[61] D. Slepian, H.O. Pollak, Prolate spheroidal wave functions, Fourier analysis and uncertainty – I, Bell Syst. Techn. J. 40 (1961) 43–63, https://doi.org/10.1002/j.1538-7305.1961.tb03976.x.
[62] H.J. Landau, H.O. Pollak, Prolate spheroidal wave functions, Fourier analysis and uncertainty – II, Bell Syst. Techn. J. 40 (1961) 65–84, https://doi.org/10.1002/j.1538-7305.1961.tb03977.x.
[63] A. Tarantola, The least-squares criterion, Inverse Problem Theory and Methods for Model Parameter Estimation, SIAM, 2005, pp. 57–80.
[64] T. Moon, W. Stirling, Signal spaces, Mathematical Methods and Algorithms for Signal Processing, Prentice Hall, Upper Saddle River, New Jersey, 2000, pp. 71–129.
[65] S. Fomel, P. Sava, I. Vlad, Y. Liu, V. Bashkardin, Madagascar: open-source software project for multidimensional data analysis and reproducible computational experiments, J. Open Res. Software 1 (2013) e8, https://doi.org/10.5334/jors.ag.